



**DEVIATION OF TIME-RESOLVED LUMINESCENCE DYNAMICS IN
MWIR SEMICONDUCTOR MATERIALS FROM CARRIER
RECOMBINATION THEORY PREDICTIONS**

THESIS

Peter M. Johnson, First Lieutenant, USAF

AFIT/GEO/ENP/04-02

**DEPARTMENT OF THE AIR FORCE
AIR UNIVERSITY**

AIR FORCE INSTITUTE OF TECHNOLOGY

Wright Patterson Air Force Base, Ohio

APPROVED FOR PUBLIC RELEASE; DISTRIBUTION UNLIMITED

THE VIEWS EXPRESSED IN THIS THESIS ARE THOSE OF THE AUTHOR AND DO NOT REFLECT THE OFFICIAL POLICY OR POSITION OF THE UNITED STATES AIR FORCE, DEPARTMENT OF DEFENSE, OR THE UNITED STATES GOVERNMENT.

DEVIATION OF TIME-RESOLVED LUMINESCENCE DYNAMICS IN
MWIR SEMICONDUCTOR MATERIALS FROM CARRIER
RECOMBINATION THEORY PREDICTIONS

THESIS

Presented to the Faculty
Department of Engineering Physics
Graduate School of Engineering and Management
Air Force Institute of Technology
Air University
Air Education and Training Command
in Partial Fulfillment of the Requirements for the
Degree of Master of Science in Electrical Engineering

Peter M. Johnson, BSEE
First Lieutenant, USAF

March, 2004

DEVIATION OF TIME-RESOLVED LUMINESCENCE DYNAMICS IN
MWIR SEMICONDUCTOR MATERIALS FROM CARRIER
RECOMBINATION THEORY PREDICTIONS

Peter M. Johnson, BSEE

First Lieutenant, USAF

Approved:

Dr. Michael A. Marciniak (Chairman)

Date

Dr. Robert A. Hengehold (Member)

Date

Dr. David E. Weeks (Member)

Date

Abstract

Time resolved luminescence spectroscopy was used to characterize luminescence decay curves for a bulk InAs sample and an InAsSb type-I quantum-well sample over the first 3ns following excitation. The luminescence decay curves were then converted to carrier densities and used to find recombination coefficients that provided the least-squared-error solution of the rate equation describing carrier recombination. Recombination coefficients describing Shockley-Read-Hall (A_{SRH}), radiative (B_{rad}), and Auger (C_{Aug}) recombination were determined at two different temperatures and four excitation powers, then analyzed for consistency and physical significance.

For all of the resulting least squares fits, a minimum of one recombination coefficient was negative. While this could be explained in terms of unconfined carriers in the quantum structure, the lack of a trend in the parameters with excitation power indicates that this was not the sole contributing factor. No explanation for this behavior could be formulated for the bulk InAs sample.

As an alternative approach, luminescence decay curves were directly analyzed to evaluate the possibility that the anomalous behavior was an artifact of the initial luminescence-to-carrier density mapping. Again, the least squares fit resulted in negative coefficients. Furthermore, when the parameters were constrained to be positive, the best fit was significantly worse than the unconstrained case. This indicated that negative parameters were not simply an artifact of noise in the data.

Because of the failure of current carrier recombination theory to adequately describe observed luminescence decay signals, further analysis of processes contributing to this deviation from theory must be evaluated. Possible nonlinearities in the experimental setup, inclusion of higher order recombination processes, or any number of other factors must be eliminated from or incorporated into the model describing luminescence decay for this approach to accurately and consistently determine recombination coefficients.

Acknowledgements

I would like to thank all those who helped me to achieve one of my highest goals. This has been the opportunity of a lifetime for me, and an experience I will never forget. The frustrations, challenges, and successes have all been a vital part of what this thesis has come to mean to me.

I owe my gratitude to many including the United States Air Force for seeing fit to give me the opportunity to pursue my educational goals unencumbered with the daily grind of the work-a-day world. My committee's support and patience were invaluable as was the support of the technical staff who helped keep the equipment up and running. I owe special gratitude to my advisor Dr. Michael Marciniak for his trust, technical help, advice, moral support, and excellent advice.

I also owe thanks to my partner Kevin for the conversation, friendship, and technical expertise he shared. The many long hours in the lab were shortened because of his innovation and skill. The conversations and discussions that we shared helped to pass the time while the experiment was running.

Above all, I need to express my deep love and gratitude for my wife and daughter. Their continual support and love have been the reinforcing strength that has allowed me to continue on. My wife's patience with unusual and unpredictable work ours, her willingness to listen to something that sounded like Greek when I needed to talk through a problem, and the warm welcoming smile at the end of a long or frustrating day were the balm that healed my broken spirit. The unfeigned love of a three-year-old, the end-of-day wrestling matches and tickle fights, and the hugs and kisses from my daughter were the glue that helped keep me together through the tough times.

I thank all who supported me through this, and hope that some day I will be able to return the favor.

Peter M. Johnson

Table of Contents

	Page
Abstract	iii
Acknowledgements	iv
List of Figures	viii
List of Tables	x
1. Introduction	1-1
1.1 Motivation	1-1
1.2 Approach	1-2
1.3 Background	1-3
1.3.1 Carrier Dynamics in Bulk Materials	1-3
1.3.2 Carrier Dynamics in Quantum Structures	1-4
1.4 Problem Statement	1-5
1.5 Overview of Results	1-5
2. Theoretical Background	2-1
2.1 Recombination Mechanisms	2-1
2.1.1 Shockley-Read-Hall Recombination	2-1
2.1.2 Radiative Recombination	2-2
2.1.3 Auger Recombination	2-4
2.2 Carrier Dynamics In Semiconductors	2-6
2.3 Carrier Dynamics In Quantum Structures	2-7
3. Experimental Technique	3-1
3.1 Experimental Setup	3-2
3.2 General Approach	3-4
3.3 Sample Descriptions	3-4

	Page
3.4 Curve Fitting and Data Analysis Techniques	3-4
3.4.1 Mapping Luminescence to Carrier Density	3-4
3.4.2 Determining A_{SRH} , B_{Rad} , and C_{Aug}	3-7
4. Results	4-1
4.1 Luminescence Decay Curves	4-1
4.2 Luminescence to Carrier Density Mapping	4-1
4.3 Re-Evaluation of Previous Data	4-4
4.4 Recombination Coefficients for Samples 94-099 and 94-052	4-5
4.4.1 Empirical Mapping	4-5
4.4.2 Theoretical Mapping	4-8
5. Conclusions and Recommendations	5-1
5.1 Conclusions	5-1
5.2 General Recommendations	5-1
Appendix A. Recommended Improvements to the Experimental Setup	A-1
A.1 Sample Mount	A-1
A.2 Stray Light	A-1
A.3 Collection Optics	A-2
Appendix B. Alignment Procedure	B-1
B.1 Alignment Laser and Pinhole Alignment	B-1
B.2 Parabolic Mirror Alignment	B-2
B.3 Sample Pump Alignment	B-3
B.4 PL Through the Pinhole and Crystal Pump Alignment	B-4
B.5 Establishing Zero Path Length	B-5
B.6 Aligning the Collection Optics	B-6
B.7 Finding and Optimizing Upconversion	B-7

	Page
Appendix C. Fundamentals of First Order Nonlinear Mixing	C-1
C.1 Conservation of Energy	C-2
C.2 Conservation of Momentum (Phase-matching)	C-3
C.3 Selmeier Equations	C-4
Appendix D. Source Code	D-1
Bibliography	BIB-1

List of Figures

Figure		Page
2.1.	Schematic representation of the three major recombination mechanisms in semiconductor materials. (a) Recombination via traps, defects, or surface states referred to as Shockley-Read-Hall recombination. (b) Radiative recombination. (c) Conduction-heavy hole-heavy hole-splitoff (CHHS) Auger recombination pathway.	2-1
2.2.	Diagram of Auger processes in a semiconductor. Processes (a), (c), (d), (f), (i), and (j) would be expected to occur in <i>n</i> -type semiconductors, while (b), (e), (g), (h), (k), and (l) would occur in <i>p</i> -type materials. Processes (a), and (b) are the only processes expected to be present in pure intrinsic materials. <i>Adapted from J. Pankove, Optical Processes in Semiconductors, Dover, 1971.</i>	2-4
2.3.	Possible band-to-band Auger recombination processes in a direct bandgap semiconductor. Similar Auger transitions are also possible for impurity-band or Donor-Acceptor recombinations. <i>Adapted from P. Bhattacharya, Semiconductor Optoelectronic Devices, Prentice Hall, 1997.</i>	2-5
2.4.	As the excitation level increases, the electron quasi-fermi level rises, and a significant portion of the free-electrons assume energies outside of the well.	2-7
3.1.	Optical sampling of the photoluminescence decay curve. A sum-frequency signal is only generated during the short time interval when the delayed pulse and the photoluminescence decay temporally overlap.	3-1
3.2.	Optical table layout for TRPL	3-3
4.1.	Typical luminescence rise time. The peak luminescence level is found by averaging five points at the top of the curve. The background level is established by blocking the beam for several data points and averaging.	4-2
4.2.	$L(n)$ mapping for the InAsSb quantum well at 77K.	4-3
4.3.	Recombination coefficients as a function of power for a type-II MWIR semiconductor sample. <i>Results obtained from data gathered by Gorski [9].</i> . . .	4-4
4.4.	Typical fit of $-dn/dt = A_{SRH}n + B_{rad}n^2 + C_{Aug}n^3$ to experimental data. The data shown is for sample 94-052 at 100K, 200mW excitation	4-5
4.5.	Recombination rate coefficients for InAs at 77K	4-6

Figure		Page
4.6.	Recombination rate coefficients for InAs at 100K	4-7
4.7.	Recombination rate coefficients for sample 94-099 at 77K	4-7
4.8.	Recombination rate coefficients for sample 94-099 at 25K	4-8
4.9.	Least squares fits for (a) Positively constrained fit parameters, and (b) Unconstrained fit parameters.	4-9
4.10.	Least squares fits for (a) Positively constrained fit parameters, and (b) Unconstrained fit parameters zoomed in on the first three ns after excitation.	4-10
A.1.	Background signal level as a function of wavelength with and without a 700nm Long-Pass filter in the crystal pump beam. Above 700nm the signal is cut off by a short pass filter placed in front of the spectrometer. . . .	A-2
A.2.	Measured PL intensity as a function of aperture diameter. The aperture was centered at the geometric focus of the second parabolic mirror in place of the nonlinear crystal.	A-3
A.3.	Measured PL intensity through a $100\mu m$ pinhole as a function of displacement in the vertical and horizontal directions.	A-3

List of Tables

Table		Page
4.1.	Results of the $L(n)$ fits. $L(n) = u_1 - u_2 e^{u_3 n}$	4-3
4.2.	Fit parameters for InAs at 100K, 200mW excitation	4-10

DEVIATION OF TIME-RESOLVED LUMINESCENCE DYNAMICS IN MWIR SEMICONDUCTOR MATERIALS FROM CARRIER RECOMBINATION THEORY PREDICTIONS

1. Introduction

Infra-Red (IR) technologies have woven their way into the fabric of both civilian and military operations. IR imaging systems have been developed for tasks ranging from target identification, characterization, and tracking to commercially available automobile night vision systems. Given the diverse number and type of applications requiring generation and detection of Mid-Wave IR (MWIR) radiation, small, robust, low-cost, and efficient sources and detectors are desirable for economical utilization of IR system capabilities.

Conventional MWIR sources are typically expensive and either bulky and fragile or incapable of producing the high power required for many military applications. The demand for smaller packages, higher output powers, and rugged designs has led to the development of narrow-bandgap semiconductor structures designed to operate in the 3 to 5 micron wavelength range.

Experimental analysis of these devices has shown that structure can play a significant role in the performance of MWIR semiconductor lasers [5, 12, 16]. An understanding of device characteristics and the physical processes that impact performance is critical to the development of more efficient, robust, and economical laser sources and detectors. This exploration will attempt to provide meaningful correlations between design parameters and processes that impact device performance by characterizing excited carrier dynamics through the use of Time-Resolved Photoluminescence (TRPL) spectroscopy.

1.1 Motivation

In recent military engagements involving the loss of aircraft due to hostile fire, IR-guided weapons have been responsible for the majority of combat-related airframe losses. For example; during the Soviet occupation of Afghanistan, roughly eighty percent of aircraft losses were attributable to IR-guided munitions [9]. Man-portable IR-guided missiles have also been used recently by terrorist organizations in attempts to down civilian aircraft [6]. To counter this

threat, the Air Force has developed the Directed Infrared Countermeasure (DIRCM) and Large Aircraft Infrared Countermeasure systems (LAIRCM).

These systems identify, track, and jam in-bound threats with appropriate MWIR radiation. One of the limiting factors for both the DIRCM and LAIRCM systems is the source of IR radiation. Currently, sources in the correct spectral range are limited to lamps such as those used on the DIRCM system, and laser sources relying on nonlinear processes to convert near-IR or long wave-IR energy to the appropriate MWIR wavelengths [20, 8]. In both cases physical considerations limit the maximum usable output power; directly impacting the standoff engagement range of the countermeasure system.

Semiconductor lasers operating in the Near-IR have proven to be compact, efficient, rugged, and cost effective with applications ranging from telecommunications to research and development. To date, MWIR semiconductor lasers have not experienced the same kind of success. However, the promise of extending the desirable characteristics of Near-IR semiconductor lasers to devices operating in the mid-IR make MWIR semiconductor lasers an attractive alternative to the sources now in use. Some progress has been made in producing high power MWIR semiconductor laser sources [12], but it is believed that a more thorough understanding of structure dependent carrier dynamics in MWIR semiconductor devices will lead to additional improvements in device performance.

1.2 Approach

This experiment will investigate excited carrier dynamics using TRPL spectroscopy. This technique, first described by Mahr [13] and described in detail by Shah [19], allows for the characterization of photoluminescence on a time scale comparable with the length of the excitation pulse. The photoluminescence data can then be used to extract carrier densities which can be fit to theoretical models describing both radiative and non-radiative carrier relaxation processes in the sample.

1.3 Background

1.3.1 Carrier Dynamics in Bulk Materials. In general, carrier recombination dynamics can be described by a differential carrier lifetime τ and recombination rate R where

$$\frac{1}{\tau} = \frac{\partial R}{\partial n} \quad (1.1)$$

If a power series solution of the form

$$R(n) = A_1n + A_2n^2 + A_3n^3 + \cdots + A_mn^m \quad (1.2)$$

is assumed, the differential carrier lifetime is then

$$\frac{1}{\tau} = A_1 + A_2n + A_3n^2 + \cdots + A_mn^m \quad (1.3)$$

where n is the excited carrier density. If defect recombination, bi-molecular (radiative) recombination, and other recombination mechanisms each contribute to only one term in the power series, the coefficients can be used to characterize the individual recombination processes in the material. Given these assumptions, A_m describes the average rate of occurrence for each the m -body recombination mechanisms. The first term in the series is generally taken to encompass defect, trap, and surface recombination processes, otherwise known as Shockley-Read-Hall recombination. The second term encompasses radiative processes and can be interpreted as the Einstein coefficient for the material. The remainder of the terms in the series arise from recombination processes involving more than two carriers.

For most MWIR semiconductor systems Shockley-Read-Hall and three body Auger recombination processes dominate the non-radiative carrier relaxation pathways. Using this assumption, the series can be truncated to the first three terms [15], resulting in

$$-\frac{dn}{dt} = A_{SRH}n + B_{rad}n^2 + C_{Aug}n^3 \quad (1.4)$$

For a given material, the coefficients are determined solely by the physical characteristics of the sample material and can be used to directly compare two different compositions or fabrication processes.

1.3.2 Carrier Dynamics in Quantum Structures. TRPL has been used in the past to characterize quantum structures in terms of the A_{SRH} , B_{rad} , and C_{Aug} coefficients [9, 5, 11]. However, the generated results have proven to be inconsistent, and at times, apparently unphysical. Gorski used this technique to study multiple quantum well structures producing coefficients which initially were thought to accurately describe recombination processes in the sample [9]. However, further analysis of the fitting routine showed that the optimum fit to the data occurred when the recombination coefficients were allowed to go negative [21]. Under the assumptions inherent in Equation 1.4, a negative coefficient would represent carrier generation via Shockley-Read-Hall, radiative, or Auger processes, which is not physically realizable. This result can, however, be explained by closer examination of carrier dynamics in quantum structures.

One example illustrating the effect of quantum confinement on the power series coefficients was published by Chen [5]. Chen studied the effect of barrier height and well width on the measured A_{SRH} , B_{rad} , and C_{Aug} coefficients by testing four samples with known differences in well width or confinement structure using the differential carrier lifetime technique [15].

To observe the effect of well width on recombination rates, two samples with 80Å and 120Å $\text{In}_{0.25}\text{Ga}_{0.75}\text{As}$ single quantum wells were fabricated. With the exception of the well widths, the two samples were indistinguishable. The effect of barrier height was observed by testing two samples with identical 70Å thick $\text{In}_{0.2}\text{Ga}_{0.8}\text{As}$ wells with different barrier configurations. The first sample utilized 2000Å graded $\text{Al}_x\text{Ga}_{1-x}\text{As}$ ($0.2 < x < 0.65$) barriers, and the second was grown with 1000Å GaAs barrier layers.

Chen observed that the carrier lifetime, τ_d , was strongly dependent on both well depth and width. To account for this, he analyzed the carrier density in the conduction band and concluded that even under low carrier injection conditions, a considerable portion of the free carriers were not confined in the quantum structure. These unconfined carriers are free to occupy a much larger volume of the sample, producing much lower carrier densities. Because of the lower carrier densities, the higher order terms of the rate equation can be dropped and the carrier lifetime in the barrier material is limited primarily by defect recombination. The barrier material then acts as a reservoir, feeding additional carriers into the well as the confined carriers relax into their equilibrium states. Because of their nature, these effects will be strongly dependent on the excitation level and corresponding initial carrier density.

Another example of this type of behavior was observed by Pikal [18]. Pikal performed analysis on quantum-well lasers in a manner similar to Chen and included an analysis of the effects of carrier storage on recombination coefficients. By accounting for unconfined carriers, Pikal was able to extrapolate the true recombination coefficients from the measured data. As a result, he observed effective rate coefficients and the true recombination coefficients that varied by as much as a factor of 300.

1.4 Problem Statement

Luminescence decay curves from a type II multiple quantum-well structure taken previously at AFIT were re-analyzed, and two samples including a bulk InAs sample and an InAsSb quantum-well were characterized in terms of the A_{SRH} , B_{rad} , and C_{Aug} parameters at varying temperatures and excitation levels using TRPL spectroscopy. The resulting parameters were then evaluated for physical significance and any trends with excitation.

1.5 Overview of Results

In all cases, the minimum squared error solution to the recombination rate equation incorporated negative coefficients. When the data for the type II sample was plotted as a function of excitation power, the B_{rad} , and C_{Aug} parameters showed negative trends with excitation power as would be expected from the results of Chen and Pikal [5, 18]. However, when the data from the InAsSb quantum-well was analyzed, the recombination coefficients oscillated about zero without exhibiting any clear trend. Additionally, the least squares solution to the recombination rate equation for the InAs bulk sample required negative coefficients. No physical explanation could be formulated that would adequately describe the behavior of the luminescence decay curves without invalidating initial assumptions about carrier dynamics in the material. Given these results, the use of TRPL spectroscopy to describe the individual recombination processes in semiconductors must be modified if the results are to accurately describe physical processes in the material.

While characterization of individual recombination mechanisms may prove difficult, the unique capabilities of this experiment to simultaneously resolve the spectral and temporal evolution of MWIR photoluminescence can be utilized in other ways. This might be done through correlating an effective luminescence decay lifetime with sample structure variations, temporally

resolving the luminescence spectra of these materials to characterize other aspects of carrier dynamics, or resolving the temporal evolution of lasing modes in MWIR semiconductor lasers.

2. Theoretical Background

Carrier dynamics in semiconductor materials can have a significant impact on device performance. In particular, non-radiative transitions reduce efficiency and contribute to device heating with all of its undesirable impacts on performance [3]. Because of this, considerable effort has gone into characterizing and mitigating the various undesirable processes in near-IR and MWIR semiconductor materials. In recent years, band engineering and advanced device structures have been devised to reduce the impacts of non-radiative processes[9]. A better understanding of the processes that impact device performance can allow for educated design tradeoffs and facilitate non-traditional solutions.

2.1 Recombination Mechanisms

In semiconductor materials, Shockley-Read-Hall recombination, radiative recombination, and Auger recombination account for the majority of relaxation pathways [17]. Briefly, Shockley-Read-Hall recombination accounts for recombination due to defects, surface states, or deep-level traps, radiative recombination is the source of light emitted from the device, and Auger recombination accounts for multi-carrier interactions that can result in non-radiative recombination. A schematic illustration of the three processes is shown in Figure 2.1.

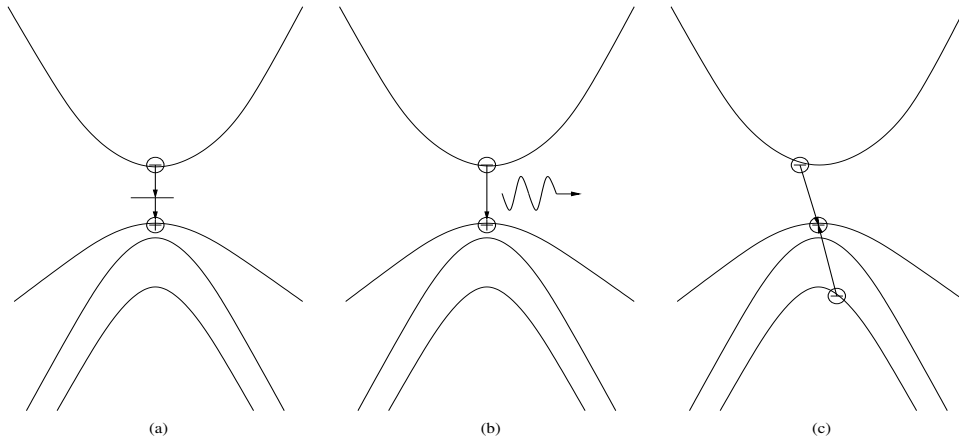


Figure 2.1 Schematic representation of the three major recombination mechanisms in semiconductor materials. (a) Recombination via traps, defects, or surface states referred to as Shockley-Read-Hall recombination. (b) Radiative recombination. (c) Conduction-heavy hole-heavy hole-splitoff (CHHS) Auger recombination pathway.

2.1.1 Shockley-Read-Hall Recombination. The Shockley-Read-Hall theory of recombination describes any non-radiative recombination pathway involving an energy level in the

semiconductor bandgap where a free carrier relaxes into the energy level via phonon emission, then relaxes to the ground state through additional phonon emissions. These relaxation pathways are generally caused by deep-level traps, surface states, or impurities in the semiconductor sample, and tend to be spatially localized. Because of this localization, they have a characteristic interaction length or cross section associated with their ability to “reach out” and capture free carriers.

The general theory of Shockley-Read-Hall recombination gives the recombination rate associated with these relaxation pathways as

$$R_{SRH} = s_r v_{th} N_T \frac{np - n_i^2}{n + p + 2n_i \cosh(\frac{E_T - E_{Fi}}{k_B T})} \quad (2.1)$$

where E_T is the trap energy level, E_{Fi} is the intrinsic Fermi level, s_r is the recombination cross section of the trap, v_{th} is the carrier thermal velocity, N_T is the recombination center density, n_i is the intrinsic carrier concentration in the material, n is the electron density, and p is the hole density [3]. For intrinsic materials, $n = p$, and the expression can be re-written as

$$R_{SRH} = s_r v_{th} N_T \frac{n^2 - n_i^2}{2n + 2n_i \cosh(\frac{E_T - E_{Fi}}{k_B T})} \quad (2.2)$$

Under moderately high excitation levels, $n \gg n_i$. Additionally, most true recombination centers have $E_t \approx E_{Fi}$, allowing the cosh term to be set to 1. These two simplifications lead to

$$R_{SRH} = s_r v_{th} N_T \frac{n}{2} \quad (2.3)$$

Setting $A_{SRH} = \frac{s_r v_{th} N_T}{2}$, the final expression for the recombination rate due to Shockley-Read-Hall processes is given by

$$R_{SRH} = A_{SRH} n \quad (2.4)$$

2.1.2 Radiative Recombination. Because the main purpose of many of the semiconductor structures of interest is to generate or detect photons, the radiative recombination mechanism is of prime importance. According to the Roosbroeck-Shockley relationship, at thermal equilibrium the rate of optical carrier excitation must equal the rate of radiative recombination. This principle leads to an expression for the rate of radiative emission (recombination) in a frequency

interval $d\nu$ given by

$$R(\nu)d\nu = P(\nu)\rho(\nu)d\nu \quad (2.5)$$

where $P(\nu)$ is the probability per unit time of absorbing a photon of energy $h\nu$, and $\rho(\nu)$ is the density of photons in an interval $d\nu$ [17].

Because this relationship is for the case of thermal equilibrium, the density of photons in a given frequency interval takes the form of Planck's relation for blackbody radiation given by

$$\rho(\nu) = \frac{8\pi\nu^2\mathbf{n}^3}{c^3 \left(\exp\left(\frac{h\nu}{k_B T}\right) - 1 \right)} d\nu \quad (2.6)$$

where \mathbf{n} is the index of refraction for the material.

An expression for the absorption probability can be developed by recognizing that $P(\nu) = \frac{1}{\tau(\nu)}$ where $\tau(\nu)$ is the mean photon lifetime in the material. Putting $\tau(\nu)$ in terms of the material's absorption coefficient and substituting it into the expression for $P(\nu)$ results in the final expression for the absorption probability

$$P(\nu) = \alpha(\nu) \frac{c}{\mathbf{n}} \quad (2.7)$$

where $\alpha(\nu)$ is the spectral absorption coefficient for the material. Combining Equations 2.6 and 2.7 results in the final form of the spectral radiative emission rate at thermal equilibrium.

$$R(\nu)d\nu = \frac{\alpha(\nu)8\pi\nu^2\mathbf{n}^2}{c^2 \left(\exp\left(\frac{h\nu}{k_B T}\right) - 1 \right)} d\nu \quad (2.8)$$

To find the total number of radiative recombinations per unit time, Equation 2.8 must be integrated over the entire range of possible frequencies. A change of variable $u = h\nu/k_B T$ is made to simplify the integration. The total rate of radiative recombinations at thermal equilibrium is then

$$R = \frac{8\pi\mathbf{n}^2(k_B T)^3}{c^2 h^3} \int_0^\infty \frac{\alpha(\nu)u^2}{e^u - 1} du \quad (2.9)$$

which is constant for a given material at temperature T . To extend this expression to the case of non-equilibrium, R is multiplied by a factor that characterizes the deviation from equilibrium

conditions [17] and results in a non-equilibrium radiative recombination rate of

$$R_{rad} = \frac{np}{n_i^2} R \quad (2.10)$$

At a constant temperature, n_i is a characteristic constant of the material. Noting that $n = p$ in intrinsic materials, and defining $B_{rad} = R/n_i^2$, Equation 2.10 can be re-written

$$R_{rad} = B_{rad} n^2 \quad (2.11)$$

2.1.3 Auger Recombination. Auger recombination processes are a class of recombination mechanisms in which an excited carrier relaxes to the ground state by giving its energy up to another carrier. The newly excited carrier then relaxes to the ground state by emitting a cascade of optical-phonons, returning the system to its ground state. There are several possible combinations of energy levels that can contribute to Auger recombination. A schematic representation of possible pathways is shown in Figure 2.2.

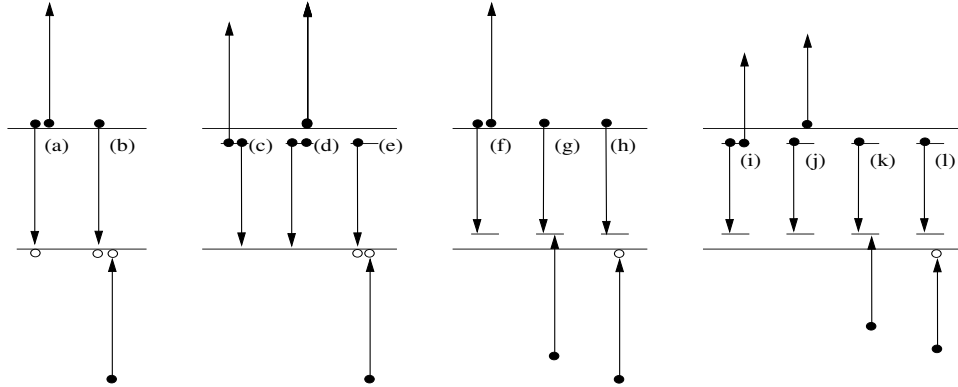


Figure 2.2 Diagram of Auger processes in a semiconductor. Processes (a), (c), (d), (f), (i), and (j) would be expected to occur in n -type semiconductors, while (b), (e), (g), (h), (k), and (l) would occur in p -type materials. Processes (a), and (b) are the only processes expected to be present in pure intrinsic materials. *Adapted from J. Pankove, Optical Processes in Semiconductors, Dover, 1971.*

For intrinsic materials, the pathways represented by (a) and (b) in Figure 2.2 are the only ones that can be expected. However, each of these processes represents an additional sub-class of recombination pathways. For example, an electron absorbing energy from a carrier in the conduction band (C) can come from the heavy hole band (H), the light hole band (L), the split-off band (S), or any of the deeper sub-bands below the valence band edge. The dominant

forms of Auger recombination in intrinsic semiconductors are shown in Figure 2.3. For MWIR semiconductors, CHHS (Conduction, Heavy hole, Heavy hole, Split-off) recombination is the most pronounced [3]. In this process, an electron in the conduction band recombines with a hole in the heavy hole band, giving its energy up to an electron in the split-off band. The carrier from the split-off band is then promoted to fill a second hole in the heavy hole band. The hole left in the split-off band by the promoted electron relaxes through phonon interactions to the top of the heavy hole band returning the system of particles to their equilibrium state.

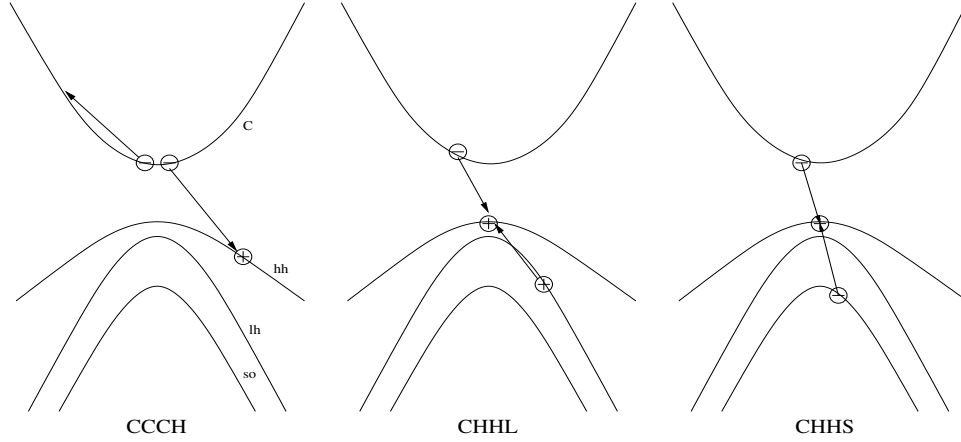


Figure 2.3 Possible band-to-band Auger recombination processes in a direct bandgap semiconductor. Similar Auger transitions are also possible for impurity-band or Donor-Acceptor recombinations. *Adapted from P. Bhattacharya, Semiconductor Optoelectronic Devices, Prentice Hall, 1997.*

A limiting constraint on Auger recombination is the requirement for conservation of momentum. In wider bandgap materials, this restriction can reduce the rate of Auger recombinations. For example, if it is assumed the light and heavy hole bands are degenerate at zone center, the CHHL interaction requires that the electron in the light hole sub-band be at an energy level approximately E_g below the top of the light hole band. Assuming a parabolic band structure, the momentum required for this electron is $\sqrt{2m_{lh}E_g}$ where m_{lh} is the electron mass in the light hole sub-band, and E_g is the bandgap of the semiconductor. Similar arguments hold true for the other sub-band interactions when the band offset is incorporated into the determination of the required energy.

Because Auger processes depend exclusively on carrier-carrier interactions, it should be intuitive that they have a direct dependence on carrier concentration. Given that the excess

carrier concentration n is proportional to

$$\left(\frac{k_B T}{E_g}\right)^{\frac{3}{2}} \exp\left(-\frac{E_g}{k_B T}\right) \quad (2.12)$$

it can be seen that the rate of Auger interactions should increase with increasing temperature and decreasing bandgap [17]. In fact, one theoretical calculation for the Auger differential lifetime that supports this concept is given by

$$\tau_{Aug} \propto \left(\frac{E_g}{k_B T}\right)^{\frac{3}{2}} \exp\left(\frac{1+2M}{1+M} \frac{E_g}{k_B T}\right) \quad (2.13)$$

where M is the ratio of electron and hole effective masses [2].

A more common approach to dealing with Auger processes is to put the recombination rate or differential lifetime directly in terms of the excess carrier concentration [10]. When this is done, the Auger lifetime and recombination rate are

$$\tau_{Aug} = (C_{Aug} n^2)^{-1} \quad (2.14)$$

$$R_{Aug} = C_{Aug} n^3 \quad (2.15)$$

2.2 Carrier Dynamics In Semiconductors

If Shockley-Read-Hall, Radiative, and Auger recombination are taken to encompass all of the significant recombination mechanisms in a semiconductor system, the overall carrier lifetime can be described by a union of the three. Combining Equations 2.4, 2.11, and 2.15, the net rate of carrier recombination can be written

$$R = A_{SRH} n + B_{rad} n^2 + C_{Aug} n^3 \quad (2.16)$$

Recognizing that $R = -dn/dt$, Equation 2.16 can be re-written as a differential equation describing the time rate of change in non-equilibrium carrier density.

$$-dn/dt = A_{SRH} n + B_{rad} n^2 + C_{Aug} n^3 \quad (2.17)$$

2.3 Carrier Dynamics In Quantum Structures

When considering recombination in quantum structures, additional factors must be accounted for. If any number of carriers are “dumped” into a one-dimensional quantum well, their energies will assume a distribution in accordance with Fermi-Dirac statistics as shown in Figure 2.4. If the barrier potential in the well is finite, the statistical distribution of the energies implies that a finite number of carriers will be free to occupy the larger volume of the barrier material. As the number of excited carriers increases, a larger and larger portion of the carrier population will be free to expand into the barrier layers. This effect has been observed in wider bandgap materials [5, 18].

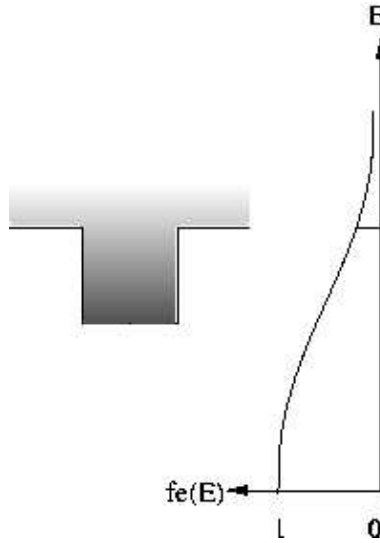


Figure 2.4 As the excitation level increases, the electron quasi-fermi level rises, and a significant portion of the free-electrons assume energies outside of the well.

After initially equilibrating, these carriers in the barrier material can relax to the ground state through relaxing into the well or through any of the recombination mechanisms previously described. This leads to a rate Equation for depopulation of the barrier material of the form

$$-dn_b/dt = A'_{SRH}n_b + B'_{rad}n_b^2 + C'_{Aug}n_b^3 + Q(n_b, n) \quad (2.18)$$

where A' , B' , and C' are the recombination coefficients for the barrier material, n_b is the carrier density in the barrier, n is the carrier density in the well, and $Q(n_b, n)$ describes the rate of relaxation into the well.

Because the volume occupied by the carriers in the barrier material is much larger than that in the wells, carrier density n_b will be much smaller, allowing Equation 2.18 to be truncated to

$$-dn_b/dt = A'_{SRH}n_b + Q(n_b, n) \quad (2.19)$$

The form of $Q(n_b, n)$ is similar to Equation 2.4 for Shockley-Read-Hall recombination. The well can be considered to have an effective capture cross section $\sigma_w(n)$, perpendicular to the plane of the confinement layer and dependent on the carrier density in the well. Under these assumptions, $Q(n_b, n)$ takes the form

$$Q(n_b, n) = \sigma_w(n)v_{\perp}n_b \quad (2.20)$$

where v_{\perp} is the component of the thermal velocity perpendicular to the confinement layer.

The carriers relaxing into the well from the barrier material add a net negative term to Equation 2.17. Adding this term, the modified rate equation is given by

$$-dn/dt = A_{SRH}n + B_{rad}n^2 + C_{Aug}n^3 - Q(n_b, n) \quad (2.21)$$

$Q(n_b, n)$ can then be written as a power series in n , leaving the dependence on n_b in the expansion coefficients.

$$Q(n_b, n) \simeq u1(n_b)n + u2(n_b)n^2 + u3(n_b)n^3 \quad (2.22)$$

Applying this to the modified rate equation results in a final form for the recombination rate equation for the quantum well that is given by

$$-dn/dt = [A_{SRH} - u1(n_b)]n + [B_{rad} - u2(n_b)]n^2 + [C_{Aug} - u3(n_b)]n^3 \quad (2.23)$$

Solving the simultaneous differential equations describing the carrier density in the barrier material and well material is not an easy task. As an alternative method for determining the recombination coefficients for the quantum well structure, it can be noted that as the excitation level and corresponding initial carrier density decreases, the number of unconfined carriers decreases. With the decrease in unconfined carriers, the expansion coefficients of Equation 2.22 decrease. If the effective coefficients of Equation 2.23 can be determined at decreasing excitation levels, they should asymptotically approach the true values of the recombination rate coefficients.

3. Experimental Technique

Due to the inherently fast nature of electronic interactions in excited materials, special techniques must be used to resolve the dynamic behavior of the energetic carriers. Streak cameras and pump-probe measurements are the most direct methods to quantify the carrier dynamics, but require experimental setups that limit their application to the UV through Near-IR portion of the spectrum.

This experiment will utilize an alternative technique called Time-Resolved Photoluminescence (TRPL) spectroscopy which leverages nonlinear mixing both to shift the generated signal into the easily detectable red or near-IR portion of the spectrum and to obtain the required temporal resolution.

First described by Mahr [13], this technique uses an ultrafast laser both to excite the sample and probe its carrier dynamics as shown in Figure 3.1. The sample is excited by a sub-picosecond pulse, producing an excitation dependent initial carrier density in the sample. These carriers cool to a quasi-equilibrium state within a few tens of picoseconds after excitation, then begin to relax toward equilibrium through both radiative and non-radiative recombination processes. The result is a photoluminescence signal that decays over a time interval on the order of several nanoseconds.

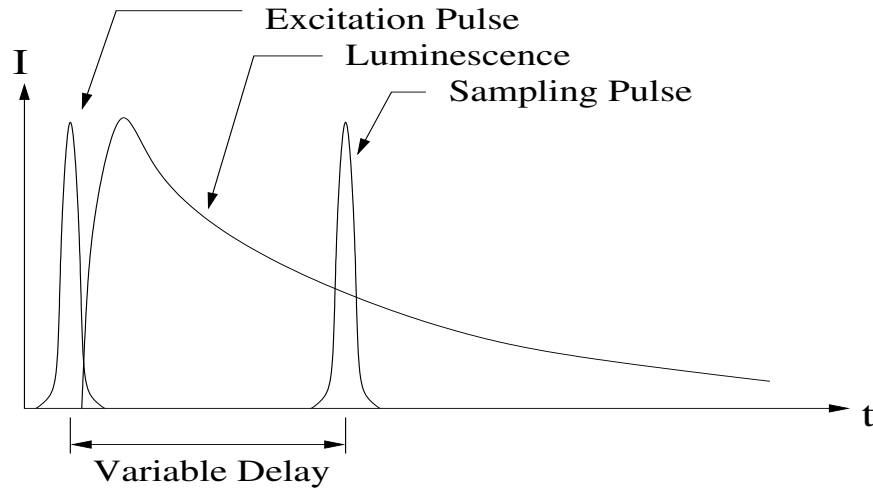


Figure 3.1 Optical sampling of the photoluminescence decay curve. A sum-frequency signal is only generated during the short time interval when the delayed pulse and the photoluminescence decay temporally overlap.

The carrier dynamics are probed by effectively sampling the photoluminescence decay curve using nonlinear mixing. To accomplish this, a portion of the pulse used to excite the

sample is delayed relative to the nonlinear crystal excitation pulse. The relative time delay between the sample and crystal excitation pulses determines the time in the decay to be probed. Both the crystal excitation pulse and the photoluminescence are focused onto a nonlinear crystal and the two beams are mixed producing a sum frequency signal amplitude that is proportional to the intensity of the photoluminescence signal at the desired time. The delay is then adjusted, and the process repeated. Using this method, the temporal behavior of the photoluminescence can be resolved to roughly the width of the excitation pulse.

Because the photoluminescence signal strength is directly dependent on the carrier density, a mapping between carrier density and photoluminescence intensity can be developed to allow the measured photoluminescence intensities to be converted to carrier densities for further analysis.

3.1 *Experimental Setup*

The experimental setup is shown in Figure 3.2. A sub-picosecond, high-intensity pulse is split into two paths using a polarizing beam splitter. The vertically polarized path, referred to as the photoluminescence leg, is shortened by a predetermined amount using a translation stage and retro-reflector, then focused onto the sample to create excited carriers. The photoluminescence generated as the excited carriers relax to the ground state is collected and collimated using an off-axis parabolic mirror, then focused onto a nonlinear crystal using a second off-axis parabolic mirror.

The horizontally polarized path, referred to as the Pump leg, is directed to and focused on the nonlinear crystal such that it temporally and spatially overlaps the focused photoluminescence beam. The nonlinear crystal is selected and oriented such that the photoluminescence and pump wavelengths produce phase-matched-sum frequency generation in the crystal.

The sum-frequency photons are then collected and focused into a $\frac{3}{4}m$ Spex monochromator and photomultiplier tube configured for photon counting and integrated to generate sufficient signal levels. The delay stage is then moved to introduce a different relative delay, and the process is repeated until the delay-range of interest has been covered.

A Spex 500M $\frac{1}{2}m$ spectrometer configured with an InSb detector is used to determine the peak luminescence wavelength, and is also used as a diagnostics tool during system alignment.

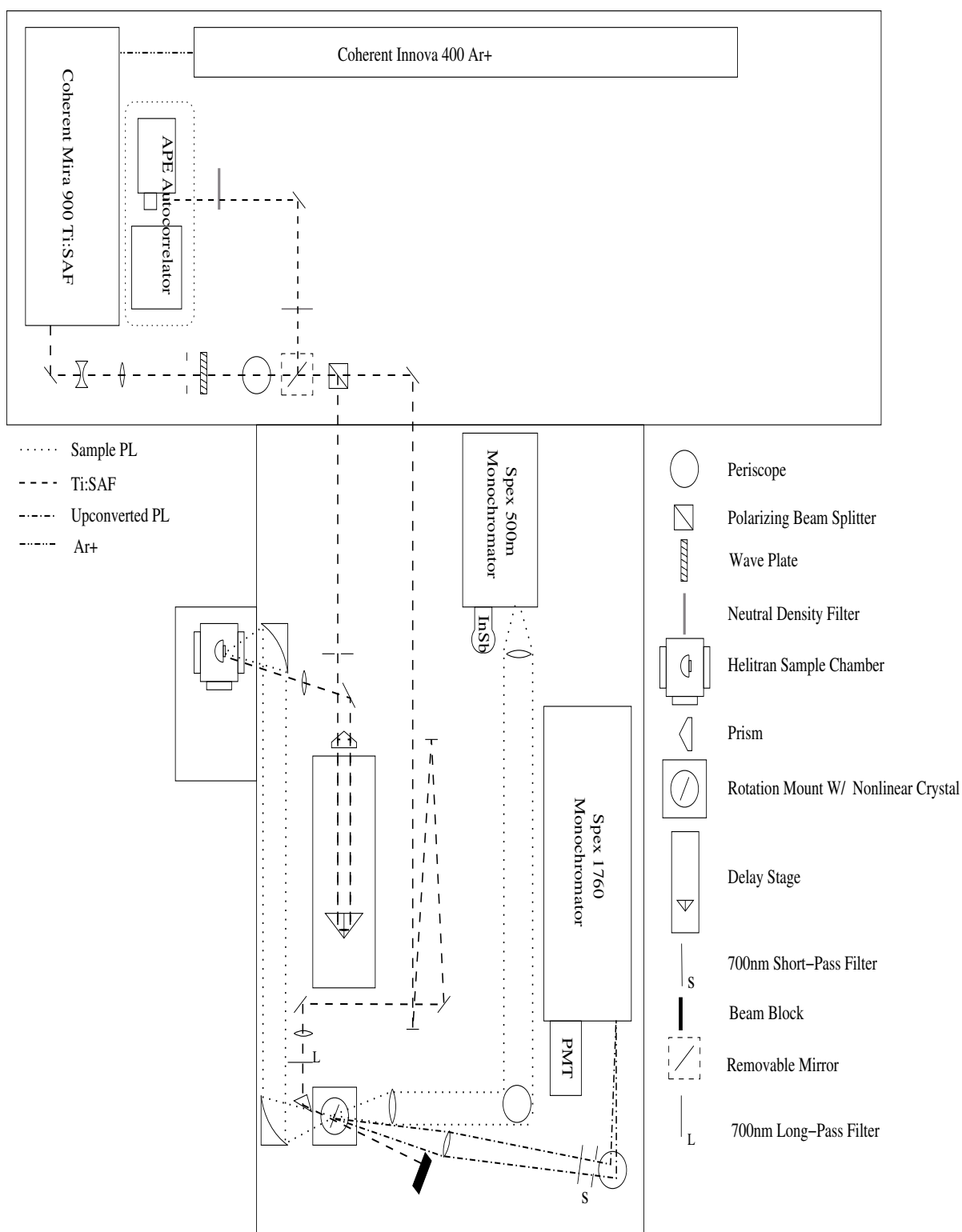


Figure 3.2 Optical table layout for TRPL

3.2 General Approach

Photoluminescence decay curves for an InAs bulk sample and an InAsSb type-I quantum well structure were measured at varying temperatures ranging from liquid helium to 100K for excitation levels ranging from 25mw to 250mw. The decay curves were then used to determine A_{SRH} , B_{rad} , and C_{Aug} recombination coefficients.

3.3 Sample Descriptions

Two MWIR semiconductor samples were tested. Sample 94-052 was epitaxially grown intrinsic InAs on an InAs substrate. The thickness of the epitaxially grown layer was unknown. Sample 94-099 was a ten-well, 135Å InAs_{0.9117}Sb_{0.0883} type-I quantum well structure with 321Å In_{0.88}Al_{0.12}As_{0.878}Sb_{0.122} barriers on a GaSb substrate.

3.4 Curve Fitting and Data Analysis Techniques

3.4.1 Mapping Luminescence to Carrier Density. Before the measured decay curves can be analyzed, they must be converted from measured luminescence to carrier density. The initial carrier densities can be calculated based on the physical constants of the experiment. These initial carrier densities can then be used in conjunction with the corresponding luminescence data to obtain the function that maps measured luminescence to carrier density.

3.4.1.1 Calculating Initial Carrier Density. Given an excitation pulse of energy E , the number of photons in the pulse is given by

$$N_{ph} = \frac{E}{h\nu} \quad (3.1)$$

For thick bulk materials, the thickness of the sample is much greater than the inverse of the absorption coefficient α , so the number of carriers generated falls off exponentially throughout the thickness of the material. As an approximation, the distribution of the carriers along the thickness direction of the sample is taken to be a flat-top distribution that cuts off at the e^{-1} point. This results in a total number of carriers in the bulk material given by

$$N_{total} = N_{ph} (1 - R_s) (1 - e^{-1}) \quad (3.2)$$

Where R_s is the reflectance of the sample. If the bulk material consists of a thin film of thickness t_f , the thickness of the film is used and the total number of carriers is given by

$$N_{total} = N_{ph} (1 - R_s) (1 - e^{-\alpha t_f}) \quad (3.3)$$

For quantum structures, both the barrier and well materials absorb photons and thereby contribute to the overall carrier density. To account for this, the thicknesses of the well and barrier materials are added, resulting in an expression for the total number of carriers in the quantum structure

$$N_{total} = N_{ph} (1 - R_s) \left(1 - e^{-\alpha N_{qw} (t_w + t_{barrier})}\right) \quad (3.4)$$

where α is the effective absorption coefficient for the well/barrier combination, N_{qw} is the number of quantum wells in the sample, t_w is the thickness of the quantum well, and $t_{barrier}$ is the thickness of the barrier material.

Once all the carriers have cooled from their high initial energy state, the initial carrier density can be calculated if it is assumed that the carriers have not significantly diffused beyond the illuminated area and that the carriers are completely confined in the wells. Given a pump beam spot size of w_p , the volume in the sample occupied by the carrier population for quantum well structures is given by

$$V = \frac{t_w \pi w_p^2}{2.6} \quad (3.5)$$

where a factor of 0.65 was added to account for the Gaussian shape of the excitation pulse.

To adapt this expression for thick bulk materials, the thickness of the wells is replaced by the absorption length $1/\alpha$ and results in a volume given by

$$V = \frac{\pi w_p^2}{2.6\alpha} \quad (3.6)$$

For thin bulk materials where $t_f < 1/\alpha$, the thickness of the wells is replaced by the thickness of the material film and results in a volume given by

$$V = \frac{t_f \pi w_p^2}{2.6} \quad (3.7)$$

Combining Equations 3.1, 3.2, and 3.6, the initial volumetric carrier density for bulk materials is

$$n(t_o) = \frac{E}{h\nu} \frac{2.6\alpha}{\pi w_p^2} (1 - R_s) (1 - e^{-1}) \quad (3.8)$$

Combining Equations 3.1, 3.4, and 3.5, the initial volumetric carrier density for quantum structures is

$$n(t_o) = \frac{E}{h\nu} \frac{2.6}{N_{qw}\pi w_p^2 t_w} (1 - R_s) \left(1 - e^{-\alpha N_{qw}(t_w + t_{barrier})}\right) \quad (3.9)$$

Combining Equations 3.1, 3.3, 3.7, the initial volumetric carrier density for thin films is

$$n(t_o) = \frac{E}{h\nu} \frac{2.6}{t_f \pi w_p^2} (1 - R_s) (1 - e^{-\alpha t_f}) \quad (3.10)$$

3.4.1.2 Determining the Carrier Mapping Relationship. Given the definition of radiative recombination in a semiconductor, the number of photons generated in a unit volume is equal to number of radiative recombinations in that same unit volume. Mathematically expressed,

$$\frac{\partial^2 P}{\partial V \partial t} = B_{rad} n^2 \quad (3.11)$$

where P is the number of photons in the volume of interest V . Recognizing that luminescence is the time rate of change in the number of photons for the case of interest, Equation 3.11 can be re-written as

$$\frac{\partial L}{\partial V} = B_{rad} n^2 \quad (3.12)$$

Assuming that the carrier density across the excited sample volume is constant, and accounting for losses including reflections at the semiconductor-air interface, the luminescence exiting the sample is given by

$$L = \frac{\eta_{ext} B_{rad} n^2}{V} \quad (3.13)$$

where η_{ext} accounts for all losses related to extracting photons from the sample.

Adding an additional term to account for collection, conversion, and detection efficiencies of the experimental system, the relationship describing measured sample luminescence is given by

$$L_s = \frac{\eta_{sys} \eta_{ext} B_{rad} n^2}{V} \quad (3.14)$$

Combining η_{sys} , η_{ext} and V , Equation 3.14 can be written

$$L_s = \eta_{eff} B_{rad} n^2 \quad (3.15)$$

Accounting for any background signal level, L_{bg} and solving for carrier density as a function of luminescence, the final mapping between carrier density and measured luminescence is given by

$$n(L) = u_1 (L - L_{bg})^{1/2} \quad (3.16)$$

where $u_1 = \sqrt{\frac{1}{\eta_{eff} B_{rad}}}$. Experimental data is used to determine L_{bg} and u_1 , and the expression is then used to map measured luminescence data to carrier density.

3.4.2 Determining A_{SRH} , B_{Rad} , and C_{Aug} . Once the decay curves have been converted into carrier densities, they represent solutions to the rate equation

$$-\frac{dn}{dt} = A_{SRH}n + B_{rad}n^2 + C_{Aug}n^3 \quad (3.17)$$

and can be used to determine the A_{SRH} , B_{Rad} , and C_{Aug} coefficients. If the initial carrier density is known, the three-dimensional parameter space containing A_{SRH} , B_{Rad} , and C_{Aug} can be searched for a minimum squared error. However, this places undesired emphasis on the value for the initial carrier concentration. Any noise contained in the initial carrier density would cause a poor fit because the resulting solution to Equation 3.17 is required to exactly contain the initial point. In order to account for the noise in the initial carrier density, it must be incorporated into the parameter space for the curve fit. The end result is a four dimensional parameter space that must be searched to find the minimum squared error solution.

To speed the search for the fit parameters, the initial carrier concentration n_o is taken to be the carrier concentration corresponding to 50ps delay, and an initial estimate for A_{SRH} is made based on the last part of the decay curve as described by Gorski [9] . To estimate A_{SRH} , it is assumed that after the first 2.5ns the “fast” depletion processes of radiative recombination and Auger recombination have depleted the excited population to the point that they no longer contribute significantly to the carrier decay. The data from 2.5ns delay out to 13.2ns when the

next excitation pulse arrives is then fit to a simple exponential

$$n(t) = n_o \exp(-A_{SRH}t) \quad (3.18)$$

resulting in an initial estimate for the A_{SRH} parameter. Initial estimates for the B_{rad} and C_{Aug} parameters can be theoretically determined [11], or can be estimated based on previous work with similar materials.

Once initial estimates for all four parameters have been obtained, a four-dimensional configuration space centered on the initial guess solution is set up to search for the minimum error. Numerical solutions for Equation 3.17 are obtained for each point in the configuration space using a Runge-Kutta integrator, and the sum of the square error is calculated for each solution. The parameters corresponding to the minimum squared error solution are then used as initial guesses and the process is repeated until the minimum square error solution corresponds with the initial guess. C code used to implement this fitting routine is included in Appendix D.

4. Results

4.1 Luminescence Decay Curves

Luminescence decay curves were collected at pump powers of 25mW, 50mW, 100mW, 150mW, and 200mW at temperatures of 77K and 100K for sample 94-052, and at temperatures of 6.8K, 25K, 77K, and 100K for sample 94-099. Decay curves were not taken for temperatures below 77K for sample 94-052 because the luminescence signal no longer decayed sufficiently before the next excitation pulse arrived.

4.2 Luminescence to Carrier Density Mapping

Six sets of data were analyzed to determine the mapping relations between luminescence and carrier density. The background level was established by averaging five datapoints taken with the sample photoluminescence blocked. Peak luminescence data was obtained by observing the rise-time of the luminescence curve and averaging five datapoints centered at the peak luminescence level. An example of the rise-time curves is shown in Figure 4.1.

Previously, the spot size required for Equations 3.9 and 3.8 was determined assuming a diffraction limited spot size given by $w = \frac{2\lambda f}{\pi D}$ where w is the beam radius, f is the lens focal-length, and D is the beam diameter prior to the focusing optic. This resulted in a pump beam spot diameter of $39.1\mu m$. However, when the pump beam was focused through a $50\mu m$ pinhole, a significant portion of the pump power was lost. This indicated that the assumption of a diffraction limited system was incorrect. To obtain a better estimate for the spot size, the focal spot was imaged onto a distant wall using a 19mm focal length lens. The imaged spot diameter was measured and used to calculate the true spot size.

The magnification of the imaging system, M , was found by noting that $s_i \gg s_o$ and using $1/s_i + 1/s_o = 1/f$, resulting in a total system magnification of $M = s_i/f$. The spot size measured using this method was $90 \pm 2\mu m$. This agreed well with the fractional pump power focused through a $50\mu m$ pinhole.

The initial carrier concentration was calculated using Equation 3.8 for the InAs bulk sample, and 3.9 for the InAsSb quantum-well sample. The published absorption coefficient for InAs [1] was used for both the bulk and quantum-well samples. An attempt to measure the absorption data for the quantum well was made, but physical limitations of the test equipment

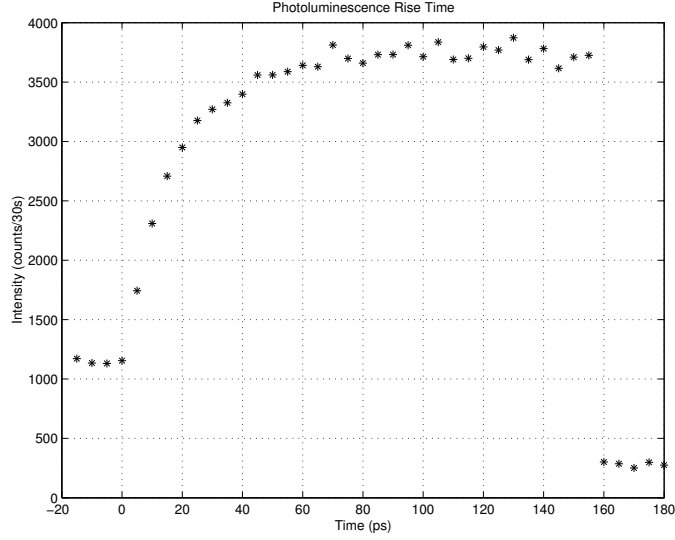


Figure 4.1 Typical luminescence rise time. The peak luminescence level is found by averaging five points at the top of the curve. The background level is established by blocking the beam for several data points and averaging.

prevented the absorption coefficient from being determined. While this impacts the scaling of the $L(n)$ mapping, the shape of the curve remains unchanged. Given that the initial carrier density scales linearly with excitation power (Eq. 3.9) the form of the $L(n)$ mapping will remain unchanged for an arbitrary change in absorption coefficient.

In all cases, the data failed to follow the trend predicted by Equation 3.11. Furthermore, two cases where the data was collected across multiple days failed to show any clear trend. This indicated that the experimental setup was sensitive to small variances in alignment introduced during startup and shutdown of the experiment. For the data sets where the data was taken in a contiguous block, the data showed a clear trend but could not be fit to Equation 3.11.

For the data sets that were gathered over a single day, the average background level was subtracted from the data, and the data was fit to an empirical relation of the form

$$L(n) = u_1 - u_2 e^{u_3 * n} \quad (4.1)$$

An example of the resulting fit is shown in Figure 4.2. The results for all of the fits are shown in Table 4.1.

While this form of mapping disagrees with Equation 3.11, it is somewhat consistent with mappings used by Gorski and others in previous works [9, 14]. In these cases, the relationship

Table 4.1 Results of the $L(n)$ fits. $L(n) = u_1 - u_2 e^{u_3 n}$

Sample	description	Temp	u1	u2	u3
94-099	InAsSb QW	77K	1320	-1310	-4.2e-19
94-099	InAsSb QW	35K	1858	-1873	-4.1e-19
94-052	Homojunction EPI InAs	77K	7440	-7610	-3.7e-19
94-052	Homojunction EPI InAs	100K	7660	-7730	-2.0e-19

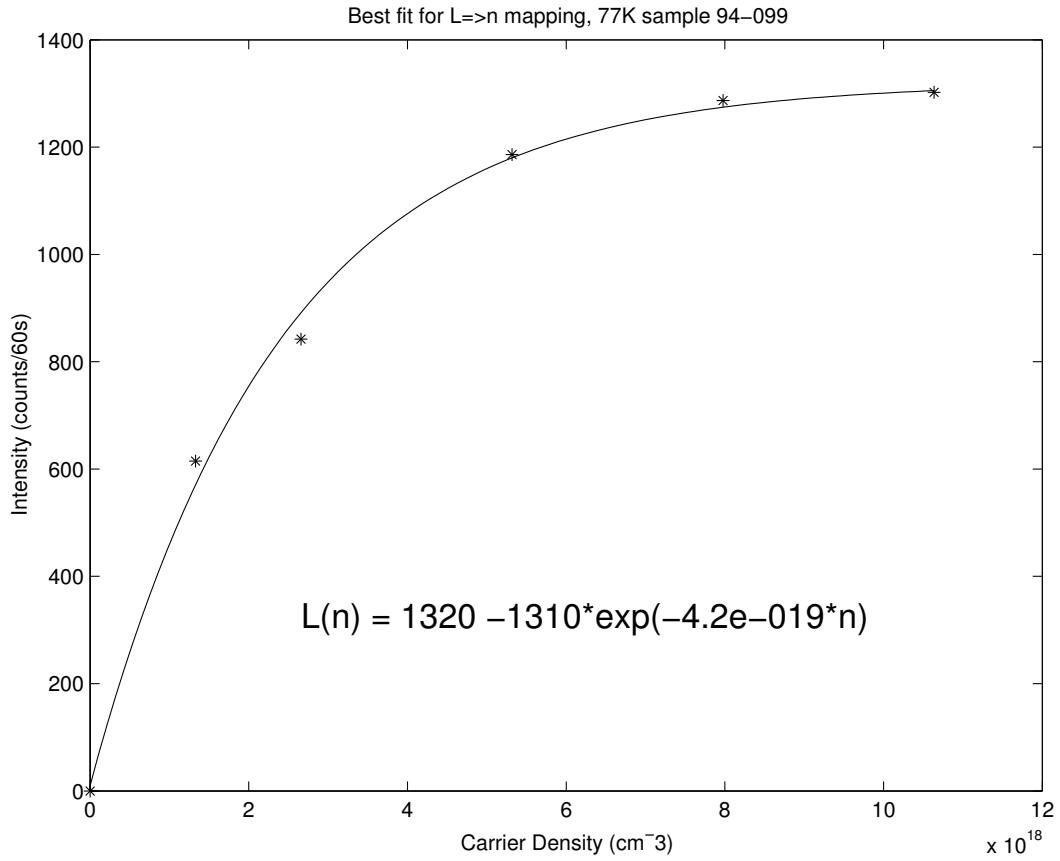


Figure 4.2 $L(n)$ mapping for the InAsSb quantum well at 77K.

between radiative recombination and detected photon flux was ignored, and the empirical mapping was assumed to accurately represent the relationship between luminescence strength and carrier density.

4.3 Re-Evaluation of Previous Data

After publication of his thesis, the results obtained by Gorski for a type-II multiple quantum well [9] were re-evaluated. Initially, Gorski constrained the recombination coefficients in the fitting routine to be positive based on the interpretation of Equation 2.17. These constraints were relaxed, and the data re-analyzed. The results of these fits are shown in Figure 4.3 and appear to support the predictions of Equation 2.23 for recombination in a quantum structure. However, the limited amount of data available prevented any error analysis on these results.

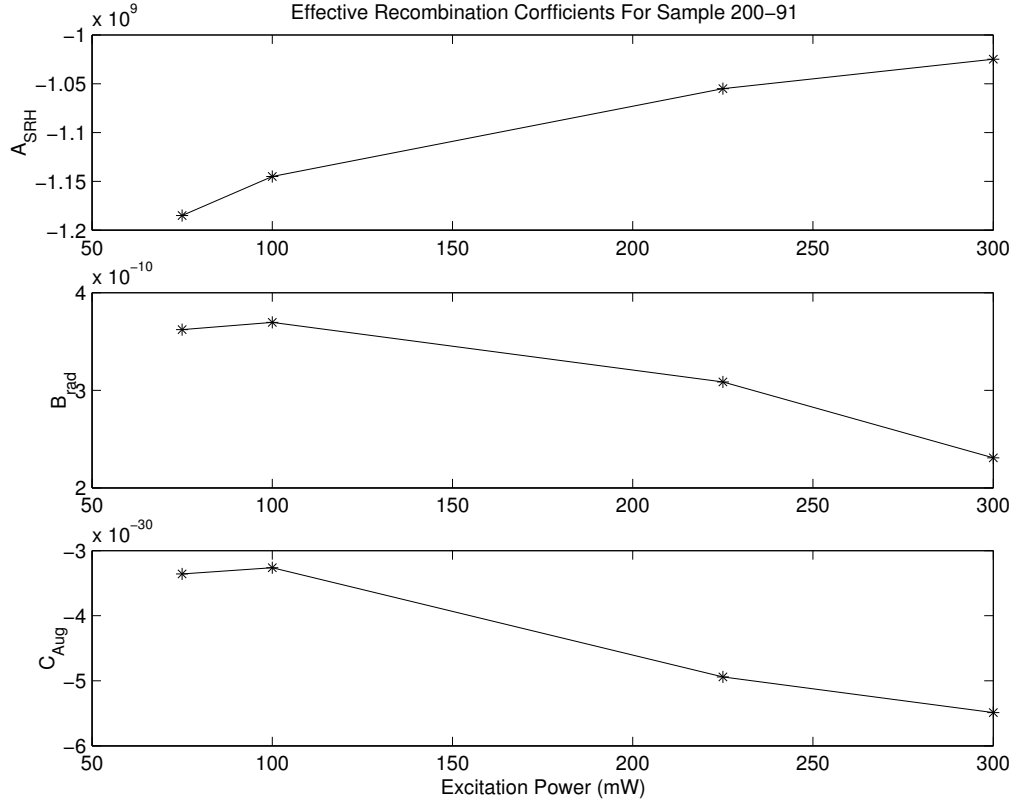


Figure 4.3 Recombination coefficients as a function of power for a type-II MWIR semiconductor sample. *Results obtained from data gathered by Gorski [9]*

4.4 Recombination Coefficients for Samples 94-099 and 94-052

4.4.1 Empirical Mapping. The photoluminescence decay curves for samples 94-099 (QW) and 94-052 (bulk) were analyzed using the empirical mappings developed previously. An example of the fit results is shown in Figure 4.4. The final results of the least-squares fits for the bulk InAs sample (94-052) are shown in Figures 4.5 and 4.6. The results of the least squares fits for the InAsSb quantum well sample (94-099) are shown in Figures 4.7 and 4.8. Once again, there was insufficient data to determine error bars.

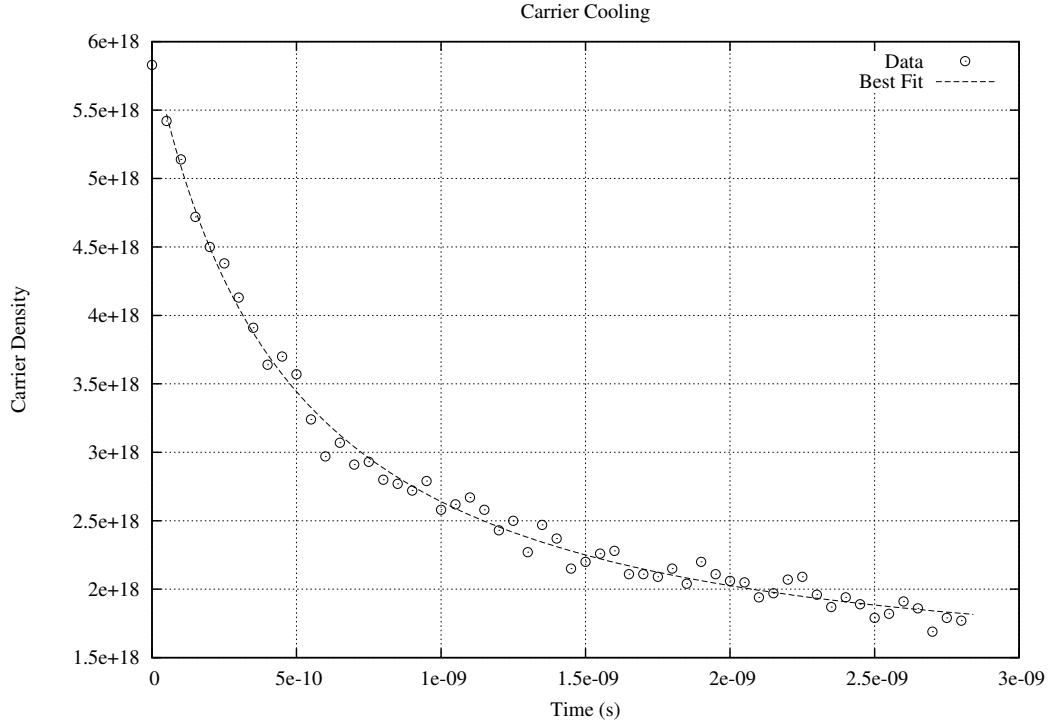


Figure 4.4 Typical fit of $-dn/dt = A_{SRH}n + B_{rad}n^2 + C_{Aug}n^3$ to experimental data. The data shown is for sample 94-052 at 100K, 200mW excitation

Of particular interest is the fact that even in the bulk sample, every excitation power and every temperature resulted in a minimum of one negative recombination coefficient. Furthermore, the apparent trends observed in Gorski's data seem to be an artifact of the variability of the fit results. Unlike Gorski's data, the quantum well sample (94-099) shows no clear trend in the recombination coefficients.

The implication of negative terms in the rate equation for bulk materials is that one or more of the required assumptions must be incorrect, or that the results are sensitive to noise in the data. Of the steps involved in the solution, the most suspect is the empirical relation

between carrier density and luminescence. The physics behind the theoretical luminescence to carrier density mapping are inherent in the basic rate equation being solved for, so a failure of the luminescence to follow this trend would imply that either the mapping or the basic rate equation is invalid.

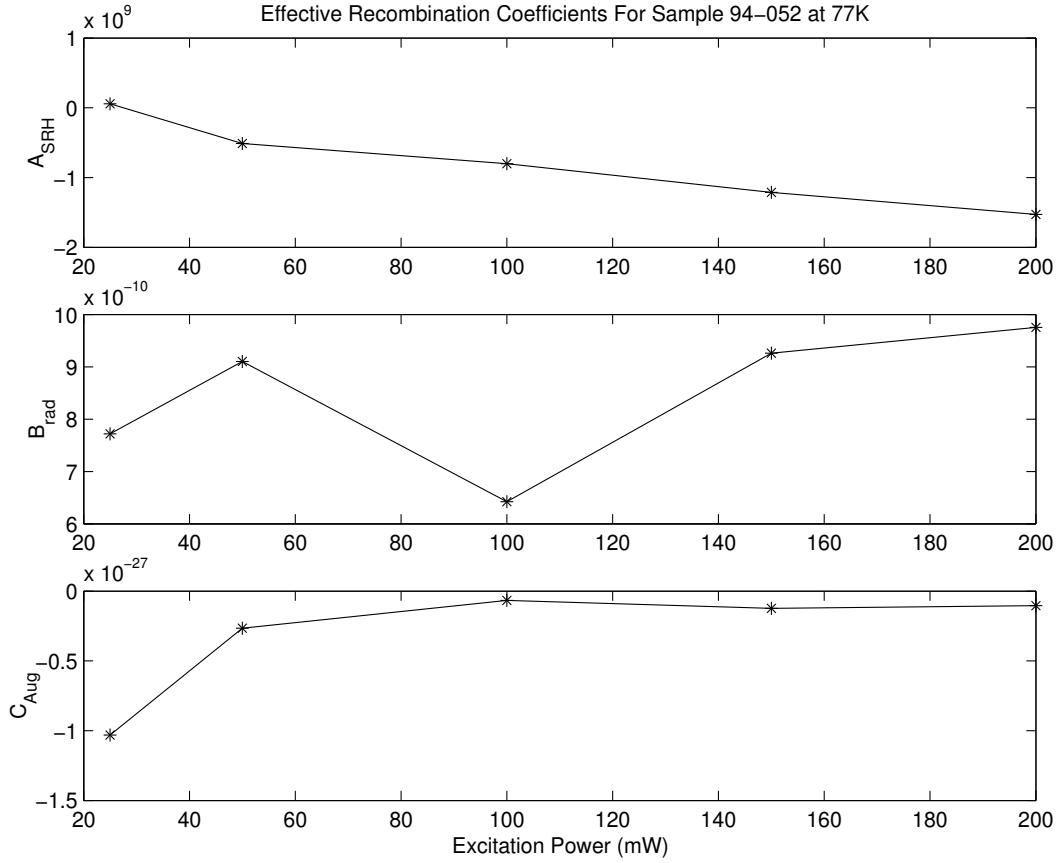


Figure 4.5 Recombination rate coefficients for InAs at 77K

Of the terms contributing to the mapping, the most ill-conditioned is the expression for the initial carrier density. Critical to the calculation are the assumptions that the carriers do not diffuse during the time it takes them to cool from their initial high-energy state to the bottom of the band edge, and that the absorption coefficient is not a function of excitation power. Additional inconsistencies arise for the case of quantum structures. In this case, the total number of excited carriers must be completely confined to the well for the calculation to be valid. Additional assumptions are that there is no absorption or transport of carriers from the substrate or cap materials into the well. Other aspects of the empirical mapping that might be suspect include the assumption that the carrier density at the peak of the luminescence curve corresponds with the initial calculated carrier density.

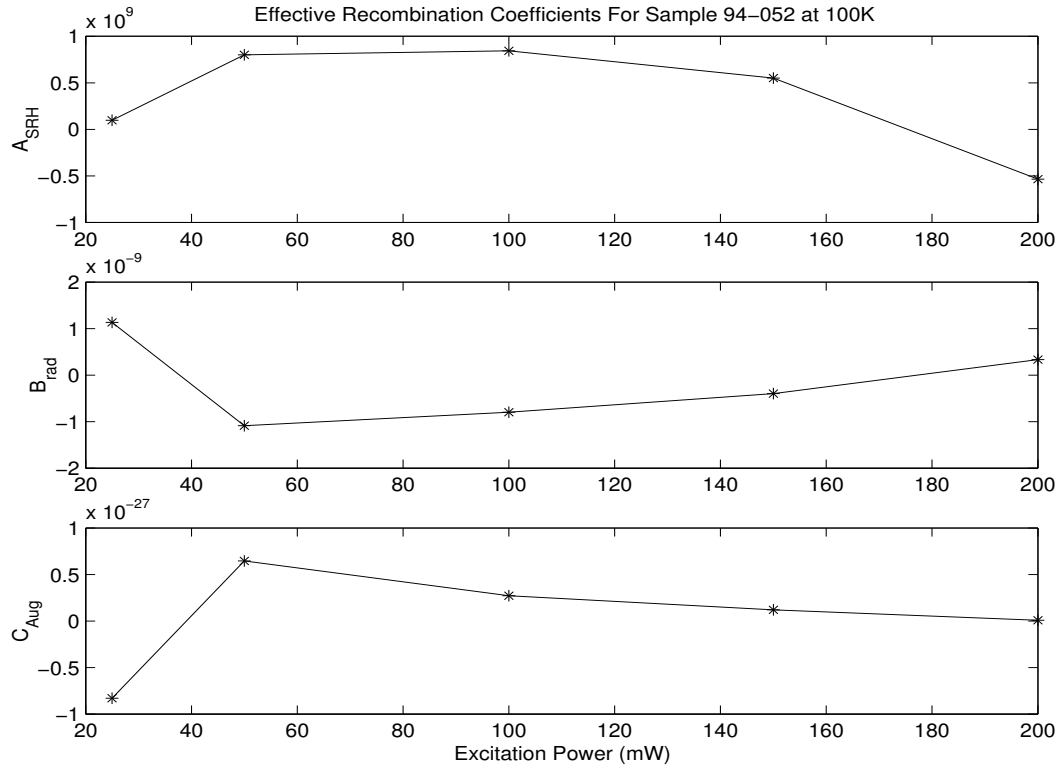


Figure 4.6 Recombination rate coefficients for InAs at 100K

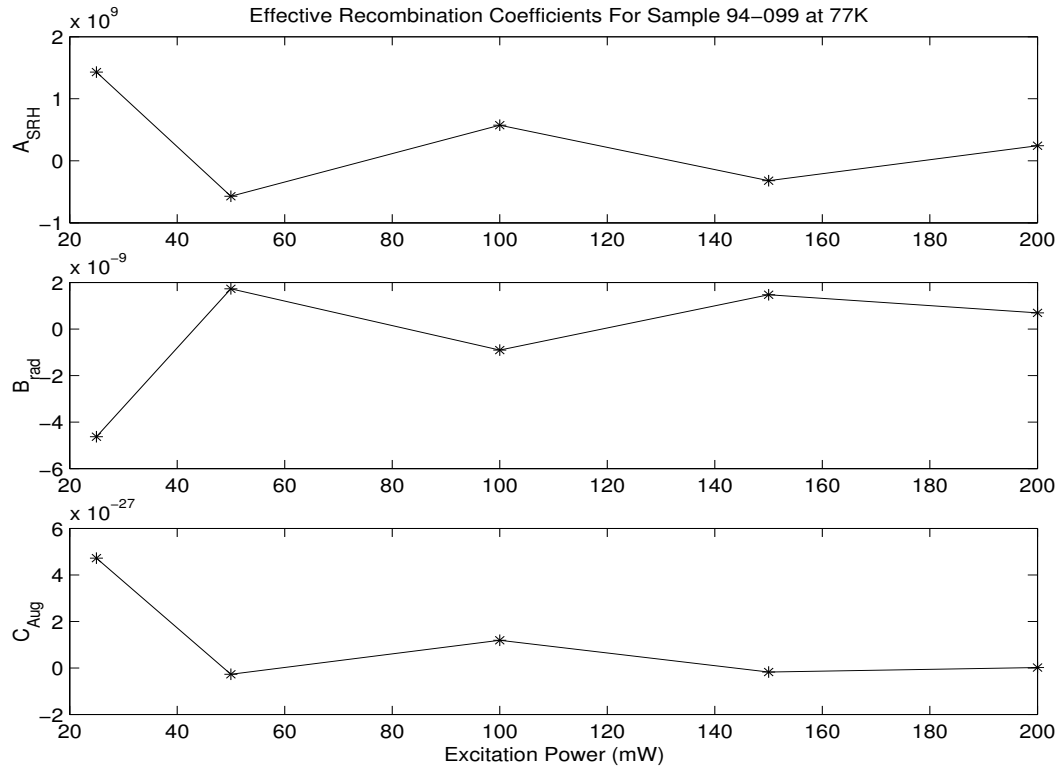


Figure 4.7 Recombination rate coefficients for sample 94-099 at 77K

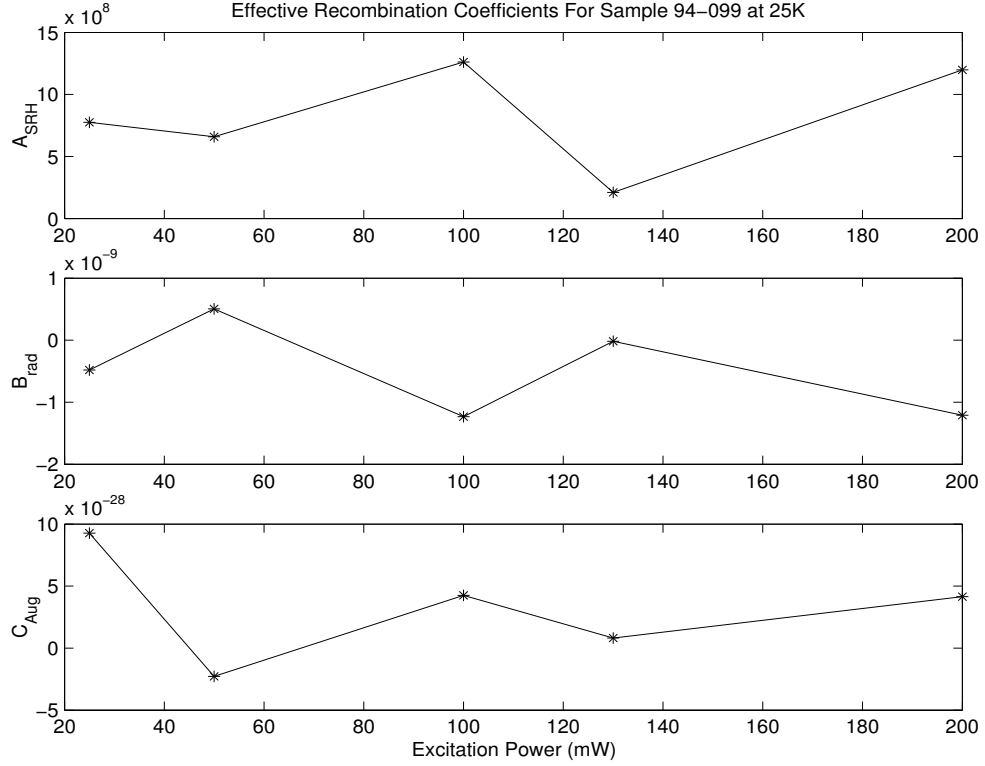


Figure 4.8 Recombination rate coefficients for sample 94-099 at 25K

4.4.2 Theoretical Mapping. To evaluate the empirical mapping's effect on measured recombination coefficients, Equation 3.16 was used to re-write the recombination rate equation in terms of instantaneous luminescence. This results in a differential equation describing luminescence decay in terms of recombination coefficients given by

$$-dL/dt = c_1 L + c_2 L^{3/2} + c_3 L^2 \quad (4.2)$$

where $c_1 = 2A_{SRH}$, $c_2 = \sqrt{B_{rad}/\eta_{eff}}$, and $c_3 = C_{Aug}/(\eta_{eff}B_{rad})$. Unfortunately A_{SRH} , B_{rad} , and C_{Aug} cannot be determined without knowing the value of η_{eff} . However, all of these terms should be positive and constant in a bulk sample for a given temperature, so the solution for c_1 , c_2 , and c_3 should be sufficient to determine if the empirical mapping of luminescence to carrier density is at fault for the erratic and seemingly unphysical nature of the resulting recombination coefficients.

The luminescence decay curve for the bulk InAs sample at 200mW excitation and 100K was fit to Equation 4.2 in the same manner as the previous fits. Unfortunately, it was found that several different orders of magnitude for c_2 and c_3 resulted in fits with roughly the same

minimum squared error, all of which would decay to near zero before the luminescence reached the data corresponding to 13.2ns after excitation. Because all of the data between 3ns and 13ns was missing, the few datapoints at the end of the decay did not contribute significantly enough to the sum squared error to force the fit to approach those values. In order to provide leverage for these points, the fit was started at the end of the decay curve and run backwards to zero delay with the initial condition fixed at the average of the last four datapoints.

Initially, the c_i coefficients were constrained to be positive by using a logarithmic scale for the search algorithm. A second fit was then done with the constraints removed to allow for negative coefficients. The results of the two fits are shown in Figures 4.9, and 4.10. Once again, the minimum squared error solution required negative coefficients. Furthermore, the constrained solution deviated from the measured data significantly enough that it no longer was contained within an envelope describing noise in the data. Additionally, the constrained fit drove two of the coefficients to the smallest number possible given the available precision, effectively setting them to zero. If the negative coefficients were simply an artifact of noise in the data, both the absolute minimum solution and the constrained minimum solution would be expected to “look” roughly the same and stay within the noise envelope.

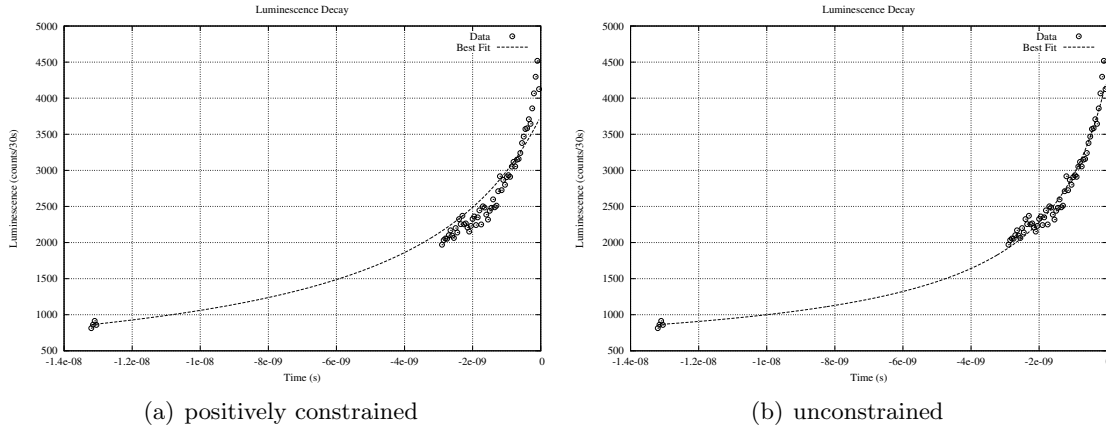


Figure 4.9 Least squares fits for (a) Positively constrained fit parameters, and (b) Unconstrained fit parameters.

The fit parameters corresponding to the best fit for both cases are contained in Table 4.2. It is notable that the sum squared error for the constrained case is significantly higher than for the unconstrained case. Additionally, the values for c_1 and c_2 correspond to the smallest positive number possible using double precision floating point calculations and the step size of

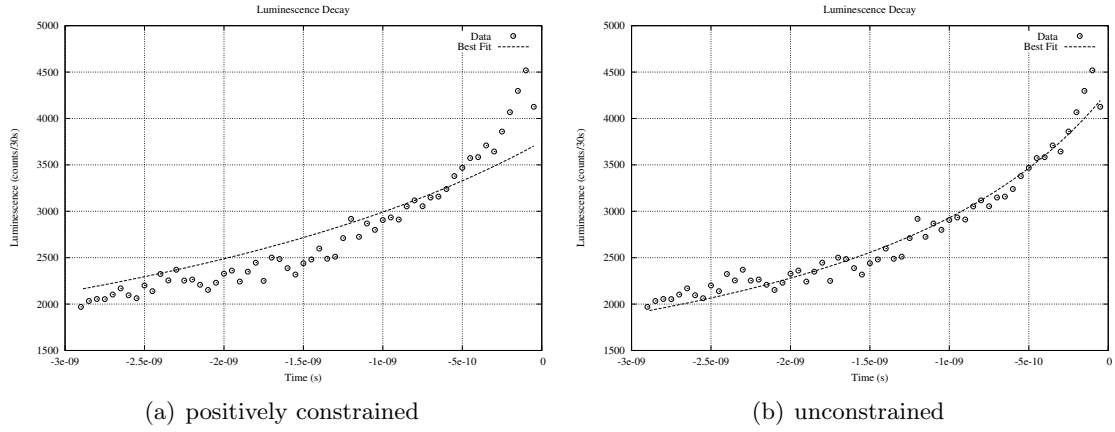


Figure 4.10 Least squares fits for (a) Positively constrained fit parameters, and (b) Unconstrained fit parameters zoomed in on the first three ns after excitation.

the search pattern. This indicates that further improvement in the fit would require negative fit parameters.

Table 4.2 Fit parameters for InAs at 100K, 200mW excitation

Fit	c_1	c_2	c_3	Sum Squared Error
Constrained	3.45846e-323	3.45846e-323	2.02908e+06	3.67073e+03
Unconstrained	2.0394e+07	-2.5701e+07	5.4648e+06	7.12322e+02

5. Conclusions and Recommendations

5.1 Conclusions

The results presented in Chapter 4 indicate that a good fit to the rate equation $-dn/dt = A_{SRH}n + B_{rad}n^2 + C_{Aug}n^3$ cannot be achieved without allowing for negative coefficients. Furthermore, given the interpretation of A_{SRH} , B_{rad} , and C_{Aug} , negative coefficients in bulk materials represent a process that is physically un-realizable.

Additional inconsistencies that limit the usefulness of this technique for characterizing individual recombination processes include the failure of measured luminescence as a function of excitation power to agree with theoretical predictions. This failure indicates that either the calculation of initial carrier density in the material is incorrect, or that the rate of radiative recombinations follows statistics different from those predicted by $-dn_{rad}/dt = B_{rad}n^2$.

If the calculation of initial carrier density were solely at fault for negative coefficients, applying the fitting routine to $-dL/dt = c_1L + c_2L^{3/2} + c_3L^2$ should have resulted in least squares fits with strictly positive coefficients. However, this was shown not to be the case. A good fit to the luminescence rate equation was impossible with positively constrained coefficients. Additionally, noise in the data was shown not to be the major contributing factor for negative coefficients.

Possible explanations for this behavior include a deviation of radiative recombination from the n^2 prediction, significant contributions from undescribed higher order processes, or an unexplained and unquantified nonlinear transfer characteristic of the test equipment. Without knowing the impact of these effects on system performance and analysis, it seems unlikely that TRPL spectroscopy can be used effectively to determine recombination coefficients.

5.2 General Recommendations

If TRPL spectroscopy is to be used to quantify recombination mechanisms, a better theoretical understanding of carrier dynamics in a given sample must be developed. Additionally, the characteristics of the test equipment must be determined using a luminescence source of known behavior. Once a clear understanding of radiative process in the sample has been developed, the recombination rate equation can be re-written in terms of the luminescence decay and used to analyze carrier dynamics after any nonlinear or otherwise undesirable transfer characteristics of the measurement system have been accounted for.

Although it may prove difficult to use this technique to determine characteristics of discrete recombination processes, the unique capabilities of time resolved luminescence spectroscopy allow for characterization of other material properties that would otherwise be unobtainable. Characterization of lasing mode dynamics in semiconductor laser structures is one area of interest that would be unaffected by the inconsistencies encountered in this work.

Another area that this experiment is well suited for would be determination of free-carrier lifetimes. For applications such as MWIR nonlinear optical limiters and generalized detectors, free-carrier effective lifetimes are critical parameters for device performance. This type of data is easily obtainable using TRPL spectroscopy and could aid in development of these materials and their applications.

Appendix A. Recommended Improvements to the Experimental Setup

Though a large amount of the variability in the experimental results has been removed through the use of standardized alignment and operating procedures, there are several areas where the experiment could be improved. The most significant areas in need of improvement include the mounting of the sample chamber, control of stray light, and efficient collection and focusing of the sample luminescence.

A.1 Sample Mount

The greatest source of day to day variability in the data was caused by small variations of the sample location relative to the collection optics. As currently configured, the cryostat is mounted on a jack stand that allows for significant motion of the sample. Any perturbation of the Helitran transfer tube, sample chamber, or cryogenic dewar results in a complete loss of signal. To prevent this type of behavior, a more rigid mount for the sample chamber/cryostat combination must be implemented to prevent the position of the sample from moving relative to the collection optics.

A.2 Stray Light

During operation, it was noted that noise in the data increased as the background level rose, and that the background level changed significantly with the upconversion wavelength being observed. To investigate this phenomenon, the photoluminescence signal was blocked and the background measured while the spectrometer was scanned through the region of interest. As shown in Figure A.1, the signal level varied strongly with wavelength. As a temporary fix, a 700nm Long-Pass filter was inserted in the crystal pump beam to cut out the unwanted radiation. As can be seen in Figure A.1 a significant improvement was made, but an appreciable amount of background radiation remained between 690nm and 700nm. Changing to a 750nm Long-Pass filter to provide spectral overlap with the 700nm Short-Pass filter, and moving the Long-Pass filter to cover both the sample and crystal pump beams should further improve the performance of the system.

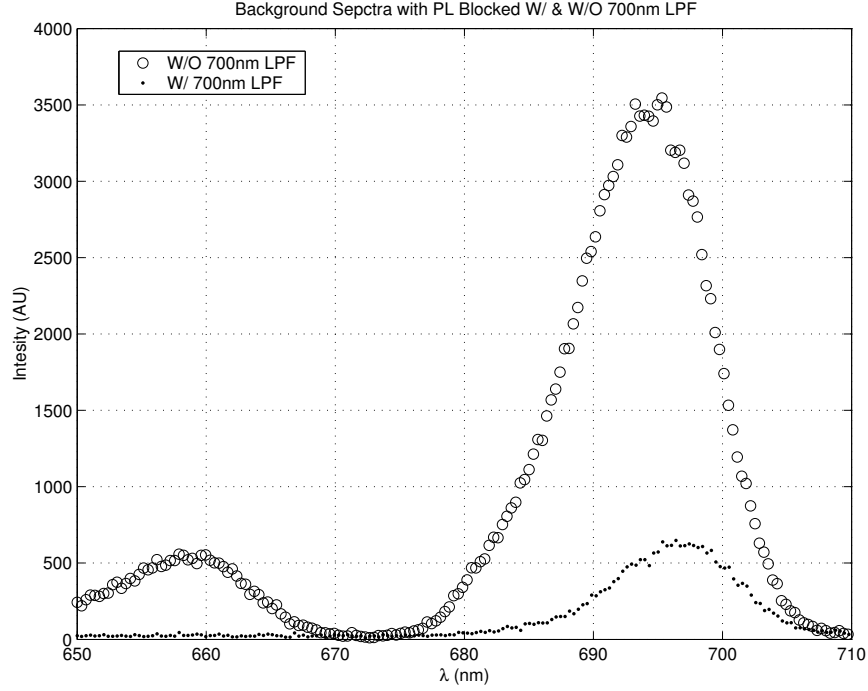


Figure A.1 Background signal level as a function of wavelength with and without a 700nm Long-Pass filter in the crystal pump beam. Above 700nm the signal is cut off by a short pass filter placed in front of the spectrometer.

A.3 Collection Optics

The primary factor limiting the ability of this experiment to characterize weakly emitting samples is the poor efficiency with which it collects, focuses, converts, and detects luminescence photons. Of these processes, collecting and focusing luminescence into the nonlinear crystal was found to be far less efficient than expected. To characterize this, photoluminescence strength was measured through an adjustable aperture centered in the nonlinear crystal mount. As can be seen in Figure A.2, a large portion of the luminescence is contained outside of a 1mm diameter circle. Given that the majority of the crystal pump beam is focused to less than $100\mu\text{m}$, only a very small percentage of the luminescence photons are available for nonlinear upconversion.

To investigate the focus of the photoluminescence beam, the PL was focused through a $100\mu\text{m}$ pinhole, which was then translated through the luminescence beam both vertically and horizontally while the signal level was monitored. It was observed that the primary lobe of the luminescence focal spot was roughly $100\mu\text{m}$ as expected, but a large portion of the signal was contained out in the wings. This spreading was particularly pronounced in the horizontal direction, and can be attributed to the nearly periodic vertical gouges left on the surfaces of

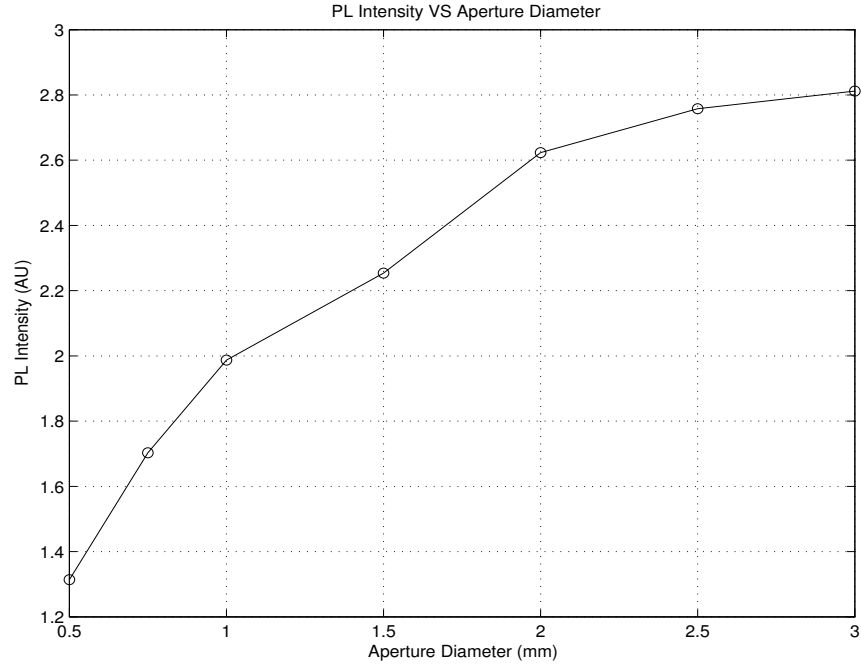


Figure A.2 Measured PL intensity as a function of aperture diameter. The aperture was centered at the geometric focus of the second parabolic mirror in place of the nonlinear crystal.

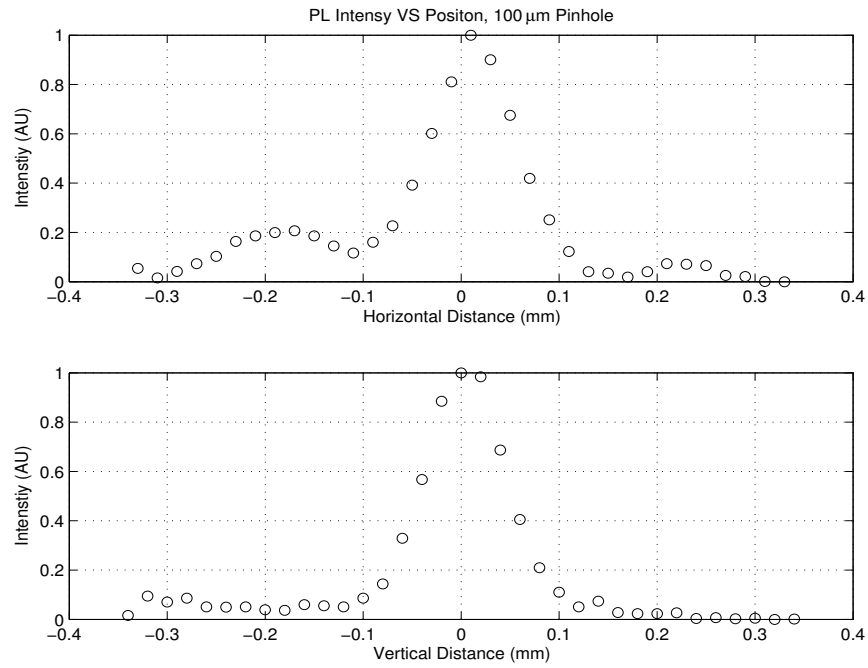


Figure A.3 Measured PL intensity through a $100\mu\text{m}$ pinhole as a function of displacement in the vertical and horizontal directions.

the parabolic mirrors by the manufacturing process. Replacing the current parabolic mirrors with more finely polished surfaces should increase the fractional photoluminescence available for upconversion, thereby increasing the sensitivity of the experiment.

Appendix B. Alignment Procedure

Historically the most difficult aspect of this experiment has been the alignment. Considerable effort went into refining the alignment procedure to remove some of the more irritating idiosyncrasies. Proper alignment requires that each of the following alignments be correct before the subsequent alignments are performed.

B.1 Alignment Laser and Pinhole Alignment

The HeNe laser is used to center the pinhole and align the parabolic mirrors, and as such its alignment is critical for a good overall system performance. For day to day operation, only the last seven steps are required. The following procedure was used to ensure proper alignment:

1. Turn on the alignment HeNe laser.
2. Lower the bottom mirror of the periscope to ensure the HeNe beam can pass unobstructed to the pinhole.
3. Remove the spatial filter and the collimating and focusing lenses from the HeNe path.
4. Mount the mirror in the rotation stage.
5. Position the mirror approximately at the center of the rotation stage.
6. Adjust the HeNe and the steering mirror so that the beam travels level with the table and perpendicular to the pinhole. (The beam will follow one line of screw holes when it is properly aligned)
7. Adjust the rotation mount so the HeNe is reflected back into the output aperture of the alignment laser and reset the zero on the rotation stage controller.
8. Mount the spatial filter without the pinhole and adjust it's height, position, and angle so that the beam is centered in the output aperture of the spatial filter and on the pinhole mount.
9. Replace the pinhole in the spatial filter and adjust it as required.
10. Mount the collimating lens and adjust it to achieve a collimated beam that is centered on the pinhole mount. Ensure that the lens is not appreciably tilted with respect to the beam propagation direction.

11. Mount the $50\mu m$ pinhole in the rotation mount.
12. Mount the focusing lens and adjust it to get maximum power through the pinhole in the pinhole mount. The beam should go roughly through the center of the focusing lens if the laser is properly aligned.
13. Rotate the pinhole mount clockwise until the beam is cut off then adjust the in-out micrometer on the rotation mount to put the beam through the pinhole again.
14. Rotate the pinhole back to zero degrees and adjust the side to side micrometer on the rotation mount to get the beam back through the pinhole.
15. Rotate the pinhole counter-clockwise until the beam is cut off again and adjust the focusing lens to put the beam back through the pinhole.
16. Repeat the last three steps until the pinhole can be rotated through the entire range without changing the observed pattern or being cut off by the pinhole. (The beam will be cut off by the mount at approximately ± 20 deg)
17. With the pinhole at zero degrees, maximize the power through the pinhole by adjusting the focus and position of the focusing lens using an optical power meter. *Note: visually maximizing the power generally leads to an incorrect focus.

B.2 Parabolic Mirror Alignment

The alignment parabolic mirrors is critical. Failure to properly align the mirrors will result in poor focus of the PL and a poor or non-existent SFG signal.

1. Complete the alignment of the alignment HeNe alignment laser and pinhole.
2. Check that the alignment beam strikes the first parabolic mirror (the mirror closest to the pinhole) in approximately the center of the mirror face. If it is off, adjust the vertical and horizontal position of the parabolic to center the beam.
3. Verify that the beam strikes the second parabolic near the center of the mirror face. If it does not, adjust the tip/tilt of the first parabolic mirror using the adjustment screws on the mirror mount to center the beam on the second mirror.
4. Place a mirror in the beam path between the two parabolic mirrors and direct it to a far wall. Observe the pattern. Adjust the horizontal and vertical controls on the first parabolic to make the beam round, and the in/out (focus) position to achieve a columnated beam.

5. Repeat the last two adjustments until the beam is both centered on the second mirror, and round/columnated.
6. Remove the cryostat from the jackstand.
7. Place the 19mm magnifying lens on the jack stand and adjust it so that all of the visible spots are centered on the lens. (The spots are caused by scattering of the beam off of the surfaces of the lens. When the lens is properly centered and oriented, all the reflections will be in the middle of the lens. The spots that appear on the front lens surface will move when the horizontal/vertical position is incorrect, and the spots appear in the center of the lens move out of center when the lens is turned away from the mirror.)
8. Translate the magnifying lens in and out to image the focal spot of the parabolic mirror on the wall. Adjust the tip/tilt of the second parabolic mirror to make the focal spot round (It may be necessary to re-position the lens to keep the beam centered). An oval or crossed focal spot indicates astigmatism that needs to be removed. Move the lens forward and back while observing the image on the wall. Check that the image is symmetric about the focal point. When the spot is round, and the image is symmetric about the focus, the mirrors are correctly aligned.

B.3 Sample Pump Alignment

This procedure aligns the sample pump to overlap the focus of the parabolic mirror and adjusts the position of the sample so that the front surface of the sample is co-located with the focus of the parabolic mirror and pump foci.

1. Align the parabolic mirrors.
2. Screw two screws into the mounting holes in the jack-stand where the cryostat bolts on to act as guides for the pinhole jig.
3. Place the pinhole jig on the jack-stand so that the recesses in the bottom of the jig fit over the top of the bolts and push the pinhole jig forward until the bolts in the jackstand are stopped up against the back of the recesses in the pinhole jig.
4. Adjust the position of the pinhole using the adjustments on the jackstand so that the alignment HeNe is focused through the pinhole. Use an optical power meter to maximize the power through the pinhole (Once again, visual maximums can be deceiving).

5. Remove the lens that focuses the pump beam onto the sample and steer the unfocused beam to the center of the pinhole mount using the steering mirror just before the focusing lens.
6. Replace the focusing lens and position it so that the beam travels through the center of the lens, and the reflection from the front surface is visible on the steering mirror mount level with the mirror to reduce any aberrations.
7. Adjust the position of the focusing lens to focus the pump beam through the pinhole. Use an optical power meter to adjust for maximum power.

B.4 PL Through the Pinhole and Crystal Pump Alignment

This procedure ensures that the PL is in fact optimally focused at the center of the rotation stage, and that the pump for the nonlinear crystal spatially overlaps the PL beam.

1. Complete all previously described alignments.
2. Block the crystal pump beam.
3. Remove the pinhole jig from the jackstand and mount the cryostat by loosely inserting the mounting screws, pushing the cryostat forward until the screws seat against the back of the mounting holes in the cryostat, and tightening the screws.
4. Adjust the position of the cryostat so that the pump beam is focused onto the sample (This is easiest with the Ti:SAF blocked and the HeNe being used as a reference). Verify that the specular reflection from the sample strikes the parabolic mirror. If not, loosen the clamps holding the jackstand to the table and rotate the jackstand/cryostat slightly so the specular reflection catches the parabolic mirror.
5. Place a beam block behind the pinhole in the rotation stage and adjust the in/out position of the cryostat so the specular reflection is focused through the pinhole. This should place the surface of the sample roughly at the focus of the parabolic mirror.
6. Raise the lower mirror of the periscope so the top of the mount is level with the black line on the post. This should position the periscope so that the PL is reflected to and focused on the spectrometer. Verify the angle of the top periscope mirror by verifying that the pump beam is focused onto the filter in front of the entrance slit on the spectrometer.

7. Fill the dewar on the InSb detector with liquid Nitrogen and allow it to cool for a few minutes. Top it off. When the detector is cool, turn on the $\pm 15V$ power supply and lock-in amplifier, then set the spectrometer to the wavelength of the sample under test.
8. Insert the chopper wheel in the path of the sample pump beam and set it for 200Hz.
9. Adjust the gain and phase of the lock in amplifier so that the signal is at least half of full scale on average. If there is no stable signal, verify that the chopper is on and in the beam, that the spectrometer is set for the correct wavelength, and that the lock-in amplifier is correctly set up.
10. Adjust the in-out position of the cryostat to obtain the best possible PL signal.
11. Adjust the position of the sample pump beam to focus the specular reflection through the pinhole.
12. Iterate the last two steps until both the optimum PL signal and pump specular reflection are observed through the pinhole.
13. Unblock the crystal pump beam and adjust the focusing lens so the pump beam is focused through the pinhole. Use an optical power meter to adjust the focusing lens to achieve maximum power through the pinhole.
14. Check the alignment by rotating the pinhole while observing the detected PL signal and the beams that are focused through the pinhole. When all is aligned correctly, the pinhole should be able to be adjusted through

B.5 Establishing Zero Path Length

Establishing Zero Path Length is an important step because it confirms the alignment, and establishes the delay that corresponds to zero path length difference.

1. Note the position of the pinhole in the rotation mount and record the reading of the in/out micrometer for future reference.
2. Replace the pinhole with the LiIO_3 crystal and move the crystal back 1.32mm to put the center of the crystal at the focal spot of the parabolic mirror. (Moving the crystal back corresponds to going to larger numbers on the micrometer)

3. Place the wave plate in the path of the crystal pump beam, rotate the crystal to approximately 18 deg and adjust the wave plate for the brightest SHG from the pump beam. This will ensure that the polarization of the pump beam is correct for phase-matching in the LiIO_3 .
4. Rotate the crystal to the angle predicted for phase matching. (Approximately between 14-18 deg)
5. While watching the output of the non-linear crystal, scan the delay stage. When the delay stage passes through zero, a blue/purple dot will be visible between the two Ti:SAF beams. Adjust the angle of the crystal and the delay to achieve maximum brightness of the SHG spot. *Note: the LiIO_3 crystal has several bad spots, it may be necessary to translate the crystal sideways a small amount to find a good spot.
6. Click on the “Zero Reset” button to set the computer’s zero to the correct spot.
7. Remove the wave plate from the crystal pump beam path.

B.6 Aligning the Collection Optics

1. Complete all previous alignments.
2. Close the spectrometer’s slits.
3. Remove the LiIO_3 crystal from the rotation mount and replace it with the mirror. Adjust the in-out position of the mirror such that it is 0.985mm in front of the position where the pinhole was centered. (Move the micrometer to a setting that is .985 larger than the setting for the pinhole)
4. Lower the bottom mirror of the periscope to allow the HeNe to strike the mirror
5. Rotate the mirror to 8 deg to reflect the alignment beam towards the collection optics.
6. Adjust the collection lens, both irises, and the filter holder, to be centered in the alignment beam. The periscope should be set already. If the periscope is not centered in the beam, translate it side to side so that it remains parallel with the spectrometer entrance slit until it is centered in the alignment beam.
7. Adjust the top mirror of the periscope to center the alignment beam on the entrance slit of the spectrometer.

8. Insert the two OD2 neutral density filters in the filter holder.
9. Set the PMT voltage to 1500 volts, turn out the room lights, and turn on the PMT power supply.
10. Set the system up to count on 0.5s, zero delay, 0ps steps, and 0mV discriminator. Start it running.
11. Slowly open the slits until a few thousand counts are registered in a half second.
12. Adjust the top mirror on the periscope and the focus of the collecting mirror for maximum counts. It may be necessary to re-adjust the spectrometer slits to prevent over exposing the PMT.
13. Adjust the first iris so the beam barely fills the collection lens, and the second iris so the beam is barely clipped by the iris to reduce stray scatter.
14. Remove the neutral density filters.
15. Turn off the PMT.
16. Fully open the spectrometer slits.
17. Remove the mirror and turn off the alignment HeNe.

B.7 Finding and Optimizing Upconversion

1. Mount the KTA crystal and position it such that it is 1.38mm behind the position where the pinhole was centered.
2. Rotate the KTA crystal to the angle required for phase-matching.
3. Ensure that the wave plate has been removed from the crystal pump beam path.
4. Position the carbon beam block such that it captures the crystal pump beam and the majority of the pump beam scatter.
5. Set the delay to 50ps, the discriminator to 50mV, the bins to 4s, and the steps to 0ps and start it running.
6. Block the PL beam and let the system run for a few counts to establish a background level.
7. Adjust the side-to-side position of the KTA crystal to minimize the background counts.

8. Stop the run and re-start it with identical settings and let it go for a few minutes to re-establish the background level.
9. Unblock the PL beam and let the system run for a few counts. Observe the difference in counts. Note that it is the signal/noise level that is of interest, and not the absolute number of counts.
10. Make a small adjustment to the parabolic in front of the nonlinear crystal and let the system run for a few counts. See if the signal is any better.
11. Block the PL beam and verify that the background is roughly where it was before.
12. Repeat the last three procedures until the signal is optimized.

Appendix C. Fundamentals of First Order Nonlinear Mixing

The contents of this appendix were adapted from reference [4] with the intent to provide the fundamental principles of nonlinear interactions required by the experimental setup. All ideas and equations are tied directly to that work.

The most direct route to understanding nonlinear interactions is to view the nonlinear crystal and incident radiation in a classical sense. In a simple model, the interaction between an incident field and a material is determined by the oscillation of a bound electron. For materials that do not exhibit nonlinear behavior this situation is adequately described by an electron in a parabolic potential whose equation of motion is that of a driven harmonic oscillator

$$\ddot{x} + \omega_0^2 x = -eE(t)/m \quad (\text{C.1})$$

where x is the electron position, ω_0 is the resonant oscillation frequency, e is the charge of the electron, m is the mass of the electron, and $E(t)$ is the driving electric field incident on the material.

Under these assumptions, the response of the system is linear for any given input field, implying that the response of the system may be frequency dependent, but that the frequencies involved are not changed in the process. However, this model assumes a parabolic potential, and as such is only valid for very small fields or moderate fields in materials such as gases where interactions with nearest neighbor atoms can be ignored.

To account for the effects of non-parabolic potentials such as those in solid materials, the equation of motion must be modified to include nonlinear terms. To do this, the restoring force (time derivative of the potential), is modeled by a Taylor series expansion and is given by

$$F_{\text{restoring}} \simeq -m\omega_0^2 x - max^2 - mbx^3 - \dots \quad (\text{C.2})$$

For the case of non-centrosymmetric materials where the potential is not symmetric about the origin, the first order correction to the equation of motion can be written

$$\ddot{x} + \omega_0^2 x + ax^2 = -eE(t)/m \quad (\text{C.3})$$

where $\omega_0^2 x + ax^2$ comes from the first two terms of the Taylor series expansion and describe the asymmetric non-parabolic nature of the potential.

Once the potential has been corrected, a mathematical form for $E(t)$ needs to be included before a solution can be sought. For two wave nonlinear interactions such as the ones we are interested in, $E(t)$ takes the form

$$E(t) = E_1 e^{i\omega_1 t} + E_2 e^{i\omega_2 t} \quad (\text{C.4})$$

Given this input field, equation C.3 has no general closed form solution. However, if the driving fields are small enough that the induced displacement of the electron satisfies the condition $\omega_0 x \gg ax^2$, a perturbation expansion of the form $x = \lambda x^{(1)} + \lambda x^{(2)} + \lambda x^{(3)} + \dots$, where λ is a coupling strength between 0 and 1, can be used to find an approximate solution. Using this method as outlined in [4], it can be shown that in addition to $\pm\omega_1$ and $\pm\omega_2$, the solutions for this equation contain the frequencies $\pm 2\omega_1, \pm 2\omega_2, \pm(\omega_1 + \omega_2), \pm(\omega_1 - \omega_2)$ and 0. It is the $\pm(\omega_1 + \omega_2)$ term that is of interest to us.

Although there exist mathematical solutions that include the frequency terms of interest, additional physical constraints must be satisfied for any of the solutions to be realized. The two basic conditions are conservation of energy and conservation of momentum. To examine these two constraints, it is simpler to use a quantum picture of the properties of light.

C.1 Conservation of Energy

As with any physical system, total energy must be conserved. In nonlinear sum frequency generation, two photons of low energy are annihilated to form a third higher energy photon. Given input photons at frequencies ω_1 and ω_2 and an output photon at frequency ω_3 , conservation of energy requires that $\hbar\omega_1 + \hbar\omega_2 = \hbar\omega_3$. Factoring out the common factor of \hbar , the basic requirement can be written

$$\omega_1 + \omega_2 = \omega_3 \quad (\text{C.5})$$

This constraint sets the frequency of the output and gives sum-frequency generation its name.

C.2 Conservation of Momentum (Phase-matching)

For momentum to be conserved, the momentum of the system of particles must be the same before and after the nonlinear interaction. The photons at frequencies ω_1 , ω_2 , and ω_3 each have momentum of $\vec{k}_1 = n_1\omega_1\hat{u}_1$, $\vec{k}_2 = n_2\omega_2\hat{u}_2$, and $\vec{k}_3 = n_3\omega_3\hat{u}_3$ where \hat{u}_1 , \hat{u}_2 , and \hat{u}_3 are unit vectors in the direction of propagation of the respective photons. Applying conservation of momentum, the phase-matching condition becomes

$$\vec{k}_1 + \vec{k}_2 = \vec{k}_3 \quad (\text{C.6})$$

For the special case when all three photons have momentum vectors that are collinear, the requirement can be expressed as

$$n_1\omega_1 + n_2\omega_2 = n_3\omega_3 \quad (\text{C.7})$$

To examine the implications of equation C.7, consider the case of a material with an index of refraction that varies monotonically with ω . The phase matching condition requires that

$$n_3 = \frac{n_1\omega_1 + n_2\omega_2}{\omega_3} \quad (\text{C.8})$$

Using this result, the quantity $n_3 - n_2$ can be rewritten as

$$n_3 - n_2 = (n_1 - n_2) \frac{\omega_1}{\omega_3} \quad (\text{C.9})$$

For materials with normal dispersion, (the index of refraction increases monotonically with ω), $n_3 > n_2$ implying that the left side of equation C.9 will always be negative, and $n_1 < n_2$ implying that the right side will always be positive. Obviously both conditions can not be met, and a sum frequency signal will not be efficiently generated. A solution to this problem can be found in birefringent materials.

In general, birefringent crystals have three eigen polarizations n_x , n_y , and n_z corresponding to the index of refraction experienced by a wave polarized along the x , y , and z crystal axes respectively. For an arbitrary polarization direction, the index of refraction is described by a 3-D ellipsoidal surface. A case of more interest for phase-matching considerations is the case of a uniaxial crystal where $n_x = n_y \neq n_z$, or a system where the beams are propagated in the $x - z$ plane of a biaxial crystal where $n_x \neq n_y \neq n_z$.

In these cases, the index of refraction seen by the polarization parallel with a principal axis remains constant at n_x for uniaxial crystals or n_y for biaxial crystals and is referred to as the ordinary index of refraction.

The orthogonal polarization, on the other hand, experiences an index of refraction that is a function of the angle θ between the propagation vector \vec{k} and the x crystal axis and is given by

$$\frac{1}{n_e(\theta)^2} = \frac{\sin^2 \theta}{n_z^2} + \frac{\cos^2 \theta}{n_x^2} \quad (\text{C.10})$$

where $n_e(\theta)$ is referred to as the extraordinary index of refraction. This angle dependent index of refraction, coupled with the difference between the extraordinary and ordinary indexes of refraction, makes phase matching possible.

To accomplish phase matching, the polarizations of the input beams need to be selected such that each sees only the ordinary or extraordinary index of refraction. A typical example is referred to as ooe phase matching. In this case ooe is short-hand for ordinary-ordinary-extraordinary and can be interpreted as follows: The first letter corresponds to the polarization of the wave at frequency ω_1 , the second corresponds to the polarization at ω_2 , and the third letter corresponds to the polarization at ω_3 . Using this configuration, the condition for phase-matching can be satisfied for collinear propagation if

$$n_o(\omega_1)\omega_1 + n_o(\omega_2)\omega_2 = n_e(\omega_3, \theta)\omega_3 \quad (\text{C.11})$$

Other possible combinations of polarizations are eeo, oeo, and eoe. These are selected as required for a given crystal/wavelength combination. If non-collinear propagation is required, the same conditions hold, but the vector nature of the momentum vectors must be considered as well.

C.3 Selmeier Equations

The dispersion relation for many optical materials can be expressed in the form of Selmeier equations. These are empirical relationships that provide the dependence of the index of refraction on the wavelength of interest, and can be used to calculate the crystal orientation that will result in phase matched output. Selmeier equations for most nonlinear optical materials are readily available in the literature. Selmeier coefficients for KTA were obtained from [7].

Appendix D. Source Code

The following C code was used to perform a least squares fit of the experimental data to the rate equation $-dL/dt = u_1n + u_2n^{3/2} + u_3n^2$. It was adapted from Fortran code originally written by Dr. David Weeks. For fitting the rate equation $-dn/dt = A_{SRH}n + B_{rad}n^2 + C_{Aug}n^3$ the file `fit.c` was modified appropriately.

The configurable parameters are stored in the file `config.dat` which must reside in the same directory as the executable program. The results of the last iteration are stored in the ASCII text file `status.dat`, and the solution to the rate equation at the minimum squared error solution is stored in the file `results.dat`. The experimental data is stored in the file `data.dat`.

As written, the program maintains all three fit parameters, and the initial condition as a variable of the fit. To configure the program to “pin” one of the parameters, the number of steps for that parameter is set to 1, and the size of the step is set to zero.

This program was written for and compiled using GNU gcc and GNU Make. It has been tested on both Windows XP with Msys and RedHat Linux 9.0.

Listing D.1 Makefile for GNU make

```
# Makefile for TRPL curve fitting program
# Peter Johnson Masters Thesis

CC=gcc
CFLAGS=-O3
LIBS=-lm
SRC=main.c patchfit.c fit.c fileio.c
OBJ=main.o patchfit.o fit.o fileio.o
TARGET=trplfit

# compile rule
trplfit: $(OBJ)
    $(CC) $(CFLAGS) -o $(TARGET) $(OBJ) $(LIBS)

# dependencies
```

```

main.o : trpl.h fileio.o
patchfit.o : trpl.h fit.c
fit.o : trpl.h
fileio.o : trpl.h

# cleanup
.PHONY: clean
clean:
    rm $(OBJ) $(TARGET)

# remove object files
.PHONY2: sweep
sweep:
    rm $(OBJ) *~

```

Listing D.2 Header file containing prototypes and global variables

```

/* header file for trpl curve fitting program */

/* function prototypes */

/* parameters and fitparameters are 4 element arrays
   parameters = [a b c eta]
   fitparameters = [ai bi ci etai]
*/

void patchfit(double parameters[], double configdata[], double *smin);
void dataload(char datafile[]);
void configure(char configfile[], double parameters[], double
               configdata[]);
void fit(double fitparameters[], double *sqerror);
void digestline(FILE *datafile);
void datasave(double t2[], double L2[], char outfile[]);

```



```

/* global variables

/* make experimental data and calculated fits global to everyone */
double t1[60],L1[60],t2[360],L2[360]; /* up to 6 calculated pts per
                                         experimental data point */
int logscale; /* search the config space on a log scale if ==1 */
int datapoints; /* number of datapoints in the file */
int ratio; /* number of calculated data points between expmtl
            datapoints... must be between 1 and 6 */
int bins; /* integration time for each datapoint */

```

Listing D.3 Main function for the fitting program

```

/* Peter Johnson,
   AFIT Masters Thesis Curve Fitting Program */

/* program to search the parameter space for the best fit to the rate
   equation  $dL/dt = -(\dots)$  given initial starting guesses and
   experimental data */

#include<stdio.h>
#include<math.h>
#include"trpl.h"

int main()
{
    /* variable declarations */
    double params[4]; /* [u1 u2 u3 L0] */
    double u1f,u2f,u3f,Lf,u1s,u2s,u3s,Ls; /* loop control stuff */
    int c1,c2,maxloops; /* looping control */
    double configs[8]; /* [du1 nu1 du2 nu2 du3 nu3 dL nL] */
    double smin; /* sum squared error */

```

```

char datafile[] = "data.dat";  /* location of experimental data */
char configfile[] = "config.dat"; /* config file contains stepsize,
                                   initial guesses, and any other
                                   control parameters */

char statusfile[] = "status.dat"; /* watch status of computation */
char outfile[] = "results.dat";  /* file to store fitted curve in */
FILE *status,*out;

/* load the configuration file */
configure(configfile, params, configs);

/* load the data file */
dataload(datafile);

/* provide a failsafe break for the search loop */
c1 = 0;
maxloops = 2e4; /* set this appropriately */

smin = 1e100; /* initialize the minimum squared error */

/* put out a status file containing the number of iterations
   complete... monitor with tail -f status.dat in a terminal */
status = fopen(statusfile, "w");
if(datafile == NULL)
{
    printf("\nCould not open status file %s\n", statusfile);
    exit(1);
}
fprintf(status, "c1\tu1\tu2\tu3\tL0\terror\n");
fclose(status);

```

```

/* walk "down hill" untill you hit a flat spot */
for (c1=0;c1<maxloops;c1++)
{

    u1s = params[0];
    u2s = params[1];
    u3s = params[2];
    Ls = params[3];

    /* calculate the best fit for the current patch */
    patchfit(params, configs, &smin);

    /* store the finish values */

    u1f = params[0];
    u2f = params[1];
    u3f = params[2];
    Lf = params[3];

    /* put a ticker in the status file */
    status = fopen(statusfile, "a");
    fprintf(status, "%i\t%i\t%i\t%i\t%i\t%i\n", c1+1, u1f, u2f, u3f,
            Lf, smin);

    fclose(status);

    /* break the loop if the start and finish are the same */
    if (u1s==u1f && u2s==u2f && u3s==u3f && Ls==Lf)
        break;
}

/* output the final results to the screen */

```

```

printf("\nu1=%e\nu2=%e\nu3=%e\n",params[0], params[1],
      params[2]);
printf("L0=%e\nMinimum_squared_error=%e\n",params[3],smin);

/* fit the final results and print to a file for plotting */
fit(params,&smin);

/* open the results output file */
out = fopen(outfile,"w");
if(datafile == NULL)
{
    printf("\nCould not open output file %s\n",outfile);
    exit(1);
}

/* put the data in the file */
for(c1=0;c1<ratio*(datapoints-1);c1++)
    fprintf(out,"%e\t%e\n",t2[c1],L2[c1]);

fclose(out); /* close the output file */

return 1;
}

```

Listing D.4 File containing the file io code

```

/* this file contains all of the file io functions that are used. it
   includes 3 functions: dataload, configure, and digestline.

   dataload loads experimental data from a file where the data is in
   two column format, the first column being the time delay, and the
   second being the carrier density. additional information after the
   first two columns is thrown away, and can contain anything or

```

nothing.

configure loads the informaion in the config.dat file. It contains information including initial guesses, stepsizes, and number of steps for the parameter search.

digestline throws away the remainder of informaiton on a given line of the input file. it is used to get rid of the description informaion and any ancillary data in the file.

**/*

/-----*/*

/ function to read data from the data file */*

/ data is stored in an ascii file in two columns 10 characters wide. The first column contains the time delay, and the second contains the measured upconverted signal in counts/30s. The signal level needs to be converted to counts/s to keep units consistent. */*

#include<stdio.h>

#include<math.h>

#include"trpl.h"

void dataload(**char** filename[])

{

int datapts,cl;

FILE *datafile;

float junk,t,L;

/ open the datafile for reading */*

datafile = fopen(filename,"r");

if(datafile == NULL)

```

    {
        printf("\nCould not open data file %s\n", filename);
        exit(1);
    }

    /* read in the data */

    /* scrap the data labels on the first line */
    digestline(datafile);

    /* paranoid initialization */
    L = 0;
    t = 0;

    for(c1=0;c1<datapoints;c1++)
    {
        fscanf(datafile, "%g %g", &t, &L);
        digestline(datafile);

        t *= 1e-12; /* put t in seconds */
        L /= bins; /* put L in counts/second */
        t1[c1] = t; /* put t & L in the arrays */
        L1[c1] = L;
    }
    fclose(datafile);

    return;
}

/*-----*/

/* function to read data from the configuration file */

```

```

/* data is stored in an ascii file in two columns. The first contains
the data, the second a string describing it. The string is
ignored, but must not be longer than 80 characters and be
terminated with a newline (\n). The data must be listed in correct
order to be properly interpreted. the order is
u10          initial guess for a
u20          initial guess for b
u30          initial guess for c
L0           initial guess for n
nu1          number of steps/patch for a
du1          size of steps in a
nu2          number of steps/patch for b
du2          size of steps in b
nu3          number of steps/patch for c
du3          size of steps in b
nL           number of stpes/patch for eta
dL           size of steps in eta
logscale     set to 1 for a log scale search in da,db,dc,deta
datapoints   number of datapoints in the datafile
bins         integration time for each datapoint

*/
#include<stdio.h>
#include<math.h>
#include"trpl.h"

void configure(char filename[],double fitparams[], double config[])
{
    int c1,c2=0;
    FILE *datafile;
    char name[20],scale;

```

```

/* initialize stuff to zero (just for safety's sake) */
for (c1=0;c1<4;c1++)
    fitparams [ c1 ] = 0;

for (c1=0;c1<8;c1++)
    config [ c1 ] = 0;

/* open the datafile for reading */
datafile = fopen ( filename , "r" );
if ( datafile == NULL )
{
    printf ( "\nCould not open configuration file %s\n" , filename );
    exit ( 1 );
}

/* read in , and echo out the configuration data */

printf ( "\nConfiguration File Data:\n" );

/* load the initial guesses */
for ( c1=0;c1<4;c1++)
{
    fscanf ( datafile , "%lg %s" , &fitparams [ c1 ] , name );
    digestline ( datafile );
    printf ( "%s = %e\n" , name , fitparams [ c1 ] );
}

/* load the search parameters */
for ( c1=0;c1<8;c1++)
{
    fscanf ( datafile , "%lg %s" , &config [ c1 ] , name );
    digestline ( datafile );
}

```



```

        printf("%s=%e\n",name,config[c1]);
    }

    /* check to see if we are doing a log scale search */
    fscanf(datafile,"%d%s",&logscale,name);
    digestline(datafile);

    if(logscale == 1)
    {
        scale = 'y';
    }
    else
        scale = 'n';

    printf("%s=%c\n",name,scale);

    /* find out how many data points are in the data file */
    fscanf(datafile,"%d%s",&datapoints,name);
    digestline(datafile);
    printf("%s=%d\n",name,datapoints);

    /* get the integration time for the data */
    fscanf(datafile,"%d%s",&bins,name);
    digestline(datafile);
    printf("%s=%d\n",name,bins);

    /* close the datafile */
    fclose(datafile);

    return;
}

```

```

void digestline(FILE *datafile)
{
    fscanf(datafile,"%*[\n]");    /* Skip to the End of the Line */
    fscanf(datafile,"%*1[\n]");    /* Skip One Newline */
}

```

Listing D.5 File containing the code to set up and search a “patch” of configuration space for the minimum squared error

```

/*-----*/

/* function to search a "patch" of configuration space for a the
   minimum square error compared with the experimental data */
#include<stdio.h>
#include<math.h>
#include"trpl.h"

void patchfit(double parameters[], double configdata[], double *smin)
{
    double du1,du2,du3,dL;
    double u1[100],u2[100],u3[100],L[100];
    int nu1,nu2,nu3,nL;
    int c1,c2,c3,c4;
    double sqerror,sqerror_f;
    double u1f,u2f,u3f,Lf;
    double u1min,u2min,u3min,Lmin;
    double f_parameters[4];

    /* initialize the search area */
    for(c1=0;c1<100;c1++)
    {
        u1[c1] = 0;
        u2[c1] = 0;

```

```

    u3[c1] = 0;
    L[c1] = 0;
}

/* set the optimum results to the inital guesses */
ulmin = parameters[0];
u2min = parameters[1];
u3min = parameters[2];
Lmin = parameters[3];
sqerror = *smin;

/* set up the step sizes for the fit parameters */
du1 = configdata[1];
du2 = configdata[3];
du3 = configdata[5];
dL = configdata[7];

/* determine how many steps to take for each parameter */
/* these numbers must be even */
nu1 = configdata[0];
nu2 = configdata[2];
nu3 = configdata[4];
nL = configdata[6];

/* set up the arrays containing the locations to be searched */
/* take out the printf stuff after done debugging */

for(c1=0;c1<nu1;c1++)
{
    if(!logscale)
        u1[c1] = ulmin - du1*nu1/2 + du1*c1;
    else

```

```

    {
        double logu1 = log10(u1min);
        u1[c1] = pow(10,(logu1 - du1*nu1/2 + du1*c1));
    }
}

for (c1=0;c1<nu2;c1++)
{
    if (!logscale)
        u2[c1] = u2min - du2*nu2/2 + du2*c1;
    else
    {
        double logu2 = log10(u2min);
        u2[c1] = pow(10,(logu2 - du2*nu2/2 + du2*c1));
    }
}

for (c1=0;c1<nu3;c1++)
{
    if (!logscale)
        u3[c1] = u3min - du3*nu3/2 + du3*c1;
    else
    {
        double logu3 = log10(u3min);
        u3[c1] = pow(10,(logu3 - du3*nu3/2 + du3*c1));
    }
}

for (c1=0;c1<nL;c1++)
{
    if (!logscale)
        L[c1] = Lmin-dL*nL/2 + dL*c1;

```

```

else
{
    double logL = log10(Lmin);
    L[c1] = pow(10,(logL - dL*nL/2 + dL*c1));
}
}

/* search the configuration space for the minimum */
for(c1=0;c1<nu1;c1++)
{
    for(c2=0;c2<nu2;c2++)
    {
        for(c3=0;c3<nu3;c3++)
        {
            for(c4=0;c4<nL;c4++)
            {
                /* calculate squared error for this point */
                f_parameters[0] = u1[c1];
                f_parameters[1] = u2[c2];
                f_parameters[2] = u3[c3];
                f_parameters[3] = L[c4];

                fit(f_parameters,&sqrerror_f);

                /* check to see if smaller than current min */
                if(sqrerror_f < sqrerror)
                {
                    sqrerror = sqrerror_f;
                    u1min = u1[c1];
                    u2min = u2[c2];
                    u3min = u3[c3];
                    Lmin = L[c4];
                }
            }
        }
    }
}

```

```

        }
    }
}

/* spit out the best fit parameters */
parameters[0] = u1min;
parameters[1] = u2min;
parameters[2] = u3min;
parameters[3] = Lmin;
*smin = sqerror;
return;
}

```

Listing D.6 Function to calculate the solution to the rate equation using a Runge-Kutta integrator for a given set of fit parameters and compute the sum squared error relative to the supplied experimental data

```

/*-----*/
/* function to calculate the squared error for a given a,b,c,n0
   and a set of experimental data. Uses a Runge-Kutta integrator to
   calculate a numerical solution to the rate equation
    $-dn/dt = an + bn^2 + cn^3$  */

#include<stdio.h>
#include<math.h>
#include"trpl.h"

void fit(double fitparameters[], double *sqerror)
{
    double error;
    double k1,k2,k3,k4;

```

```

double Ltemp,L,dt,t0,tf,ddt;
int c1,datapts,calcpts;
double u1,u2,u3,L0;

datapts = 56;  /* number of datapoints */
ratio = 6;     /* number of calculated points divided by number of
                  experimental data points increase for higher
                  accuracy, decrease for faster speed */
calcpts = datapts*ratio; /* number of calculated data points */

ddt = 50e-12;  /* 50ps steps between datapoints */
dt = ddt/ratio; /* need to figure out how to get this */
t0 = t1[0];    /* time corresponding to first data point */

u1 = fitparameters[0];
u2 = fitparameters[1];
u3 = fitparameters[2];
L0 = fitparameters[3];
L = L0;        /* set the initial condition */

/* implement the Runge-Kutta integrator */
for(c1=0;c1<calcpts;c1++)
{
    Ltemp = L;
    k1 = -dt*(u1*Ltemp + u2*pow(Ltemp,1.5) + u3*Ltemp*Ltemp);
    Ltemp = L+0.5*k1;
    k2 = -dt*(u1*Ltemp + u2*pow(Ltemp,1.5) + u3*Ltemp*Ltemp);
    Ltemp = L+0.5*k1;
    k3 = -dt*(u1*Ltemp + u2*pow(Ltemp,1.5) + u3*Ltemp*Ltemp);
    Ltemp = L+k3;
    k4 = -dt*(u1*Ltemp + u2*pow(Ltemp,1.5) + u3*Ltemp*Ltemp);
    L = L+(k1 + 2*k2 + 2*k3 + k4)/6;
}

```

```

    t2[c1] = t0 + c1*dt;
    L2[c1] = L;
}

error=0; /* initialize the squared error term */

/* sum the squared error for each datapoint */
for(c1=0;c1<datapts;c1++)
{
    if(L1[c1] > 0) /* throw out negative carrier densities */
        error = error + (L1[c1] - L2[ratio*c1])*(L1[c1] - L2[ratio*c1]);
}
*sqrerror = error;
return;
}

```


Bibliography

1. Aspnes, D.E. and A. A. Studna. "Dielectric Functions and Optical Parameters of Si, Ge, GaP, GaAs, GaSb, InP, InAs, and InSb from 1.5 to 6.0 eV," *Physical Review B*, 27(2):985–1009 (January 1983).
2. Beattie, A. R. and P. T. Landsberg. "Auger effect in semiconductors," *Proceedings of the Royal Society of London*, A249(16):16–29 (1958).
3. Bhattacharya, Pallab. *Semiconductor Optoelectronic Devices* (Second Edition). Prentice Hall, 1997.
4. Boyd, R. W. *Nonlinear Optics*. Academic Press, 1992.
5. Chen, Y. C., et al. "Carrier Recombination Rates in Strained-Layer InGaAs-GaAs Quantum Wells," *IEEE Journal of Quantum Electronics*, QE-27(6):1451 (June 1991).
6. CNN. "Kenya Missile Attack Sparks New Urgency." CNN News Article 4 Dec, 2002.
7. Fennimore, D. L., et al. "Infrared Corrected Sellmeier Coefficients for Potassium Titanyl Arsenate," *Journal of the Optical Society of America B*, 12(5):794–796 (May 1995).
8. Fibertek Corp. "IRCM Laser Transmitter." <http://www.fibertek.com/ircm.asp>.
9. Gorski, S. *Carrier Dynamics in Mid-Infrared Quangum Well Lasers Using Time-Resolved Photoluminescence*. MS thesis, Air Force Institute of Technology, Wright-Patterson AFB, OH, March 2002.
10. Hill, D. and P. T. Landsberg. "A formalism for the indirect Auger effect. I," *Proceedings of the Royal Society of London, Series A (Mathematical and Physical Sciences)*, 347(1651):547–64 (1976).
11. Jang, D. J., et al. "Hot carrier dynamics in a (GaInSb/InAs)/GaInAlAsSb superlattice multiple quantum well measured with mid-wave infrared, subpicosecond photoluminescence upconversion," *Applied Physics Letters*, 70(9):1125–27 (March 1997).
12. Kaspi, R., et al. "High Power and High Brightness from an Optically Pumped InAs/InGaSb type II Midinfrared Laser with Low Confinement," *Applied Physics Letters*, 81(3):406–408 (July 2002).
13. Mahr, H. and M. D. Hirsch. "An Optical Up-Conversion Light Gate with Picosecond Resolution," *Optics Communications*, 13(2):96–99 (February 1975).
14. Mckay, M. *Time-Resolved Photoluminescence of InAs/GaInSb Quantum Well Lasers*. MS thesis, Air Force Institute of Technology, 2000.
15. Olshansky, Robert, et al. "Measurement of Radiative and Nonradiative Recombination Rates in InGaAsP and AlGaAs Light Sources," *IEEE Journal Of Quantum Electronics*, 20(8):838–854 (August 1984).
16. Ongstad, A. P., et al. "Linewidth Analysis of the Photoluminescence from InAs/GaSb/InAs/AlSb type II Superlattices," *Journal of Applied Physics*, 87(11):7896–7902 (June 2000).
17. Pankove, J. I. *Optical Processes in Semiconductors*. 180 Varick Street, New York NY, 10014: Dover Publications, Inc., 1975.

18. Pikal, J. M., et al. "Carrier Lifetime and Recombination in Long-Wavelength Quantum-Well Lasers," *IEEE Journal of Selected Topics in Quantum Electronics*, 5(3):613–619 (May 1999).
19. Shah, Jagdeep. "Ultrafast Luminescence Spectroscopy Using Sum Frequency Generation," *IEEE Journal of Quantum Electronics*, 24(2):276–288 (February 1988).
20. USAF Aeronautical Systems Center. "LAIRCM Next Generation Missile Warning Subsystem." PIXS Industry Day Notice <http://www.pixs.wpafb.af.mil/pixs>, May 2003.
21. Weeks, D. E., "Personal Communication." AFIT/ENP MWIR Semiconductor Research Group Mtg., June 2003.

REPORT DOCUMENTATION PAGE				Form Approved OMB No. 074-0188	
<p>The public reporting burden for this collection of information is estimated to average 1 hour per response, including the time for reviewing instructions, searching existing data sources, gathering and maintaining the data needed, and completing and reviewing the collection of information. Send comments regarding this burden estimate or any other aspect of the collection of information, including suggestions for reducing this burden to Department of Defense, Washington Headquarters Services, Directorate for Information Operations and Reports (0704-0188), 1215 Jefferson Davis Highway, Suite 1204, Arlington, VA 22202-4302. Respondents should be aware that notwithstanding any other provision of law, no person shall be subject to a penalty for failing to comply with a collection of information if it does not display a currently valid OMB control number.</p> <p>PLEASE DO NOT RETURN YOUR FORM TO THE ABOVE ADDRESS.</p>					
1. REPORT DATE (DD-MM-YYYY) 03-12-2004		2. REPORT TYPE Master's Thesis		3. DATES COVERED (From – To) Sep 2003 – Mar 2004	
4. TITLE AND SUBTITLE Deviation of Time-Resolved Luminescence Dynamics in MWIR Semiconductor Materials From Carrier Recombination Theory Predictions				5a. CONTRACT NUMBER	
				5b. GRANT NUMBER	
				5c. PROGRAM ELEMENT NUMBER	
6. AUTHOR(S) Johnson, Peter, M., 1Lt, USAF				5d. PROJECT NUMBER	
				5e. TASK NUMBER	
				5f. WORK UNIT NUMBER	
7. PERFORMING ORGANIZATION NAMES(S) AND ADDRESS(S) Air Force Institute of Technology Graduate School of Engineering and Management (AFIT/EN) 2950 P Street, Building 641 WPAFB OH 45433-7765				8. PERFORMING ORGANIZATION REPORT NUMBER AFIT/GEO/ENP/04-2	
9. SPONSORING/MONITORING AGENCY NAME(S) AND ADDRESS(ES) Air Force Office Of Scientific Research 801 North Randolph Street Arlington, VA 22203-1977				10. SPONSOR/MONITOR'S ACRONYM(S) AFOSR/MOA	
				11. SPONSOR/MONITOR'S REPORT NUMBER(S)	
12. DISTRIBUTION/AVAILABILITY STATEMENT APPROVED FOR PUBLIC RELEASE; DISTRIBUTION UNLIMITED.					
13. SUPPLEMENTARY NOTES					
14. ABSTRACT Previously, Time-Resolved Luminescence Spectroscopy (TRPL) has been used to quantify undesirable recombination processes in MWIR semiconductor materials that degrade laser device performance. Analysis of results obtained by AFIT in past years showed that the analysis techniques used were inadequate. Furthermore, application of unrestricted analysis techniques led to results that were unphysical given the initial assumptions of the experiment. To quantify the impact of the initial assumptions used, bulk and Type-I quantum-well MWIR semiconductor samples were characterized using TRPL and the unrestricted analysis techniques. The results showed that quantification of recombination mechanisms using this technique is not possible without incorporating additional parameters that are presently unavailable.					
15. SUBJECT TERMS Time Resolved Luminescence Spectroscopy, MIWR semiconductors, Auger Recombination,					
16. SECURITY CLASSIFICATION OF:		17. LIMITATION OF ABSTRACT		18. NUMBER OF PAGES	
REPORT U	ABSTRACT U	c. THIS PAGE U	UU	86	
				19a. NAME OF RESPONSIBLE PERSON PETER M. JOHNSON, 1Lt, USAF (ENP)	
				19b. TELEPHONE NUMBER (Include area code) (937) 255-3636, ext 6168; e-mail: Peter.Johnson@afit.edu	